

Investigating Excitation-Induced Phonons in an Erbium Quantum Memory Crystal

Adrian Schmidt

A thesis submitted for the degree of
Bachelor of Science with Honours in Physics of
The Australian National University

October, 2020

Declaration

This thesis is an account of research undertaken between February 2020 and October 2020 at The Research School of Physics, The Australian National University, Canberra, Australia.

Except where acknowledged in the customary manner, the material presented in this thesis is, to the best of my knowledge, original and has not been submitted in whole or part for a degree in any university.

Adrian Schmidt

October, 2020

Acknowledgements

I think, unlike most of the world, I was mentally prepared for the year from hell. I was anticipating being locked away for months, unable to get a haircut, visit the gym, or go to the pub - I was doing physics honours! Well... I guess that was truer than expected. Even with the current global context, this whole experience was smoother than expected, and I attribute that fully to the people who helped and supported me throughout this process.

I thank Rose Ahlefeldt and Matt Sellars for supervising me. I started the year asking Rose if she had any projects that were a little experimental, a little theoretical, and a little bit of programming. With such a vague description, Rose organised a fulfilling project that ticked all those boxes. Rose has been so generous with her time, explaining concepts, answering questions, and thoroughly proof-reading my submissions (if I didn't do them the day before they were due). Matt's help in guiding the project ensured that I was always heading in the right direction. I admire his breadth of knowledge, creative solutions, and really wish I took his electronics course when I had the chance. I feel incredibly lucky to have such helpful and supportive people looking over my project - I would have really struggled without supervisors like Rose and Matt. I also thank James Stuart, who made the original observations this project is based on and helped me run my experiments. I am incredibly appreciative for the many days James spent in the lab with me, teaching me how to operate the experimental equipment, and even coming in on weekends to top up the liquid nitrogen. I'd also like to thank the PhD students in the group for generating a welcoming environment where I was happy to ask questions. Particular thanks to Kieran for helping me run the crystal field modelling, and Matt and James for helping proofread this thesis. I also thank John Bottega, who manufactured the sample mount incredibly quickly based off of my crude drawings.

I should also thank my friends - particularly my housemates, Joel, Henri, and (honorary housemate) Elisa. I couldn't ask for better people to play boardgames, watch movies, eat my baking, and yell at the Formula 1 with. Finally, a big thanks to my family, who continually supported me throughout this whole degree. I always looked forward to our (now socially distanced) Sunday dinner - it was a consistent source of comfort.

Abstract

Quantum memories are a key element of global quantum network designs. Ensembles of rare earth ions in crystals, and particularly erbium in the crystal Y_2SiO_5 , have been identified as good candidates for these memories. Memories made in this crystal have shown good efficiencies and storage times, however, the data storage rates are low. It is important to understand the processes that limit storage density to determine the possible data rates, and this thesis studies a particular process that will affect data storage densities in quantum memories based on $\text{Er}:\text{Y}_2\text{SiO}_5$.

This project was motivated by observations made by the ANU rare earth research group, that an excitation induced interaction was affecting the quantum memory preparation process in $^{167}\text{Er}:\text{Y}_2\text{SiO}_5$. Increasing excitation is required to increase the storage densities of quantum memories, so this process will limit data storage densities. The aim of this thesis was to use experiments to determine what this process was, and a combination of experiments and crystal field modelling to characterise it.

The effect was measured by using a laser to create excitations millimetres away from probed atoms. The distance dependence of the process was measured, and it was found that non-equilibrium phonons were being produced as the optically excited erbium decays. The frequency dependence of the process was measured by changing the frequency of the excited phonons. The phonons were measured to have an effect over a range of 2.7 GHz. Comparing this frequency width to crystal field models, the phonons are shown to match the transitions between low energy levels of the material. The propagation of the phonons across the crystal was studied. The results suggested that the phonons propagate diffusively rather than ballistically. The lifetime of the phonons processes was measured. The measurements were dominated by the lifetime of the excited state (9.2 ms). This indicates that the phonon lifetimes are significantly shorter than the optical lifetime, and no longer than 100 μs .

These findings contribute to the improvement of quantum memory storage densities in $\text{Er}^{3+}:\text{Y}_2\text{SiO}_5$ and confirm that non-equilibrium phonons need to be considered for future implementations of rare-earth based quantum memories in a quantum network.

Contents

Declaration	iii
Acknowledgements	v
Abstract	vii
1 Introduction	1
1.1 Overview and motivation	1
1.2 Thesis outline	3
2 Background Theory	5
2.1 Properties of Er ³⁺ :Y ₂ SiO ₅	5
2.1.1 Electronic structure of the rare-earths	5
2.1.2 Crystal structure	6
2.1.3 Hamiltonian	7
2.1.4 Hyperfine transitions	10
2.2 Storing Quantum Information	10
2.2.1 Two-level Systems and the Bloch Sphere	10
2.2.2 Photon echoes	13
2.2.3 Spectral preparation	15
2.2.4 The atomic frequency comb protocol	15
2.3 Interactions that effect quantum information storage	18
2.4 Chapter summary	21
3 Experimental Methods	23
3.1 Sample rod design	23
3.1.1 Experimental Setup	24
3.2 Experimental techniques	27
3.2.1 Spin polarisation	27
3.2.2 Hole burning	29
3.3 Chapter summary	31
4 Confirming phonon induced population redistribution in Er³⁺:Y₂SiO₅	33
4.1 Recreating the observed effect	33
4.2 Confirmation of phonons by translating the beam	35
4.2.1 Hole fill-in induced by the edges of the beam	36
4.3 Chapter summary	38
5 Characterisation of phonons	39
5.1 Frequency dependence of the phonon relaxation	39
5.2 Discerning the phonon type	40
5.3 Propagation properties	43

5.4	Photon echoes	44
5.5	Phonon lifetime from echoes	46
5.6	Chapter Summary	47
6	Conclusions	49
6.1	Outlook and future directions	50
	Bibliography	53

Introduction

1.1 Overview and motivation

The ability to connect quantum systems from across the world would allow for more powerful quantum computers, and communication that is much more secure than currently available [1]. To achieve these connections, a global-scale quantum network that transmits quantum information encoded onto light is needed. This is best performed by optical fibres, as in our current internet, however, even optical fibres suffer from light attenuation resulting in loss of information. This is rectified in classical systems by either directly amplifying the signal or through a measurement and regeneration procedure. Both these techniques significantly degrade any quantum information. An alternative solution is necessary for a quantum network.

Quantum repeaters are devices that regenerate a quantum signal without measuring the input. In the repeater protocol, nodes are evenly distributed along the optical network, and quantum entanglement is established between adjacent nodes via optical links. This entanglement is propagated out from one node to the next through joint measurements at the intermediate nodes. This procedure is repeated until entanglement is established between the two outermost nodes, allowing for information to be transmitted using quantum teleportation without sending photons along the network [2]. Most quantum repeater designs require the ability to store an input quantum state for a period without measurement using a device known as a quantum memory [2, 3, 4]. These memories can be made by transferring a quantum state of light onto quantum superposition states of atomic systems. This process needs to be reversible, so that the excited atoms can later emit the same input state.

A promising class of materials for holding quantum information and making quantum memories are rare-earth doped crystals. These memories collectively hold information using a large ensemble of rare-earth ions distributed throughout the crystal. A rare-earth of particular interest is erbium, as its lowest optical transition falls within the 1550nm low-loss band of optical fibres.

For practical implementation in a quantum repeater, a quantum memory would need to meet a few criteria. The input states would need to be stored for at least 100ms for a global network with a length of 10,000km [5], which has been achieved in erbium doped crystals [6]. The storage needs to be efficient, with around 90% of the input light being output [7]. Efficiencies in rare-earth crystals on the order of 70% have been achieved so far [8], but many protocols have theoretical efficiencies that meet the requirements [9] [10].

The transmission rate of the quantum repeater will depend on the data storage capacity of the memory. Currently, only five states have been stored separated in time [11], and 225 states have been stored separated in space [12]. Without improvements to the storage density of the quantum memories, the data rates of a quantum network will be severely limited [13].

Ultimately, the storage density will be limited by interactions between the ions that make up the memory. The storage-limiting interactions can be both short and long-range. For short-range interactions, optically exciting an ion changes the environment seen by nearby ions. For example, exciting an ion will change the electric field experienced by neighbouring ions, resulting in a temporary frequency shift, and loss of stored information. These interactions typically become negligible for separations beyond a few nanometres. Long range interactions involve the emission and absorption of quantised lattice vibrations (phonons). Short-range interactions are well studied in rare-earth crystals, but there has been little work done to characterise the impact of phonons in rare-earth based quantum memories.

The impact of the different interactions will depend on the method used to store more information. There are three fundamental ways of storing multiple bits of information (multiplexing): frequency, time, and spatial, as shown in Figure 1.1. Frequency and time multiplexing involve storing information in the one ensemble of atoms. The efficiencies of these storing processes are limited by both short and long-range interactions. Spatial multiplexing involves storing information over many ensembles of atoms. As these ensembles will be separated by more than nanometres, there will be no short range interactions between the multiplexed memories, however, spatial multiplexing would be affected by any long-range interactions.

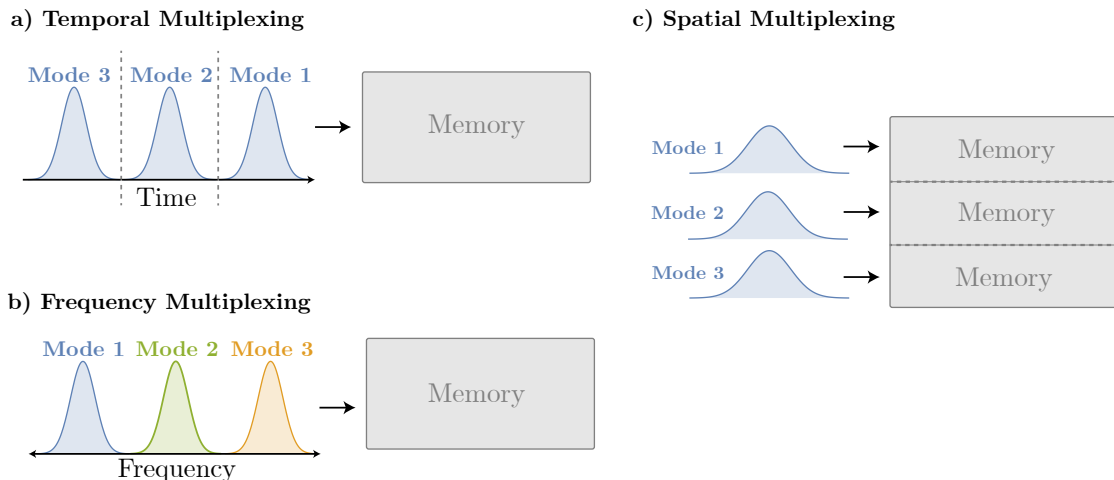


Figure 1.1: The various methods of multiplexing of a quantum memory. The three colours represent different states to be stored. In temporal multiplexing, shown in a), the modes are input separated in time. In frequency multiplexing, shown in b), they are input at different frequencies. In spatial multiplexing, shown in c), they are input at different sections of the storing medium.

Recent work in the rare-earth quantum information group at ANU suggests that more interactions may need to be considered than just the short-range interactions. A PhD researcher in our group, James Stuart, observed that during quantum memory preparation

in $\text{Er}^{3+}:\text{Y}_2\text{SiO}_5$, increasing the optical excitation made the preparation worse. It was proposed that this was due to the laser exciting atoms that emitted phonons. In this thesis I analyse the occurrence of phonons in this crystal, using experiments to confirm the effect, find what is causing them, and determine some properties of the phonons. This is an important step in improving the storage density of rare-earth crystal based quantum memories, making them more viable for future applications in a quantum internet.

1.2 Thesis outline

The structure of this thesis is listed below. Chapter 2 is background theory. Chapter 3 consists of experimental design and techniques. Chapter 4 and Chapter 5 are both original results.

In Chapter 2, I give background information that motivates the later chapters. I discuss the material being studied, $\text{Er}^{3+}:\text{Y}_2\text{SiO}_5$, covering its structure, energy levels, and transitions. I introduce a quantum memory protocol and consider the interactions that could contribute to the observed relaxation process. This information puts the work into context and introduces the interactions that are studied in this thesis.

In Chapter 3, I describe the experimental methods used in this thesis. I outline the motivation behind the experimental setup and parts I designed. I then detail the measurement methods developed for this experiment, and the calculations necessary to determine the size of the phonon effect.

In Chapter 4, I use the methods from Chapter 3 to confirm that phonons are indeed the source of the observed excitation induced effect.

In Chapter 5, I measure properties of these phonons, describing their linewidth, propagation properties, effects on coherence time, and lifetimes.

The aim of this thesis is to study a process that would affect memory performance in high storage density memories in $\text{Er}^{3+}:\text{Y}_2\text{SiO}_5$. The phonons shown to cause decoherence have not been considered as a large effect in rare-earth crystal based quantum memories, however they will be a significant constraint in a real-world implementation. My studies in this thesis are the first steps to characterising the phonons and determining methods to mitigate their effects.

Background Theory

In this chapter, I will provide background theory that motivates and explains the studies in the further chapters. I will start with the properties of the studied material, $\text{Er}^{3+}:\text{Y}_2\text{SiO}_5$. I will discuss how it can store information for long times, the structure of the crystal, the formation of its energy levels, and the transitions studied in this thesis. I will then discuss how quantum information is stored, and the principles behind a quantum memory. I follow this by describing the various interactions that could be contributing to the observed information loss. This information is key to the experimental design and analysis I perform in this thesis.

2.1 Properties of $\text{Er}^{3+}:\text{Y}_2\text{SiO}_5$

In this section I am going to discuss the electronic structure of the material, and the Hamiltonian that describes the resulting energy levels under experimental conditions. This information is important for understanding how the material is used to store quantum information, and the many interactions that potentially limit storage times. I will also discuss the structure of the crystal, as this influenced much of the experimental design.

2.1.1 Electronic structure of the rare-earths

Rare earth crystals are a common medium for quantum information storage, with good performances in coherence times [14], information densities [11], memory efficiencies [8], and multimode storage [15, 11]. These abilities can be attributed to the unique electronic structure of the rare-earths - they have the electronic structure $[\text{Xe}]4f^n$, where n is the number of electrons in the 4f shell, ranging between 1 and 14. Looking at Figure 2.1, we can see that electrons in this shell have a spatial extent smaller than the fully filled 5s and 5p shells. As a result, the valence electrons are shielded from external perturbations, such as electric or magnetic fields, or interactions with other ions in the crystal. This means that rare earth ions in crystals have transition linewidths comparable to highly isolated atoms, such as low density gases. Crystals are a useful medium for holding the rare-earth ions, as the ions are separated from each other, and maintain a constant position.

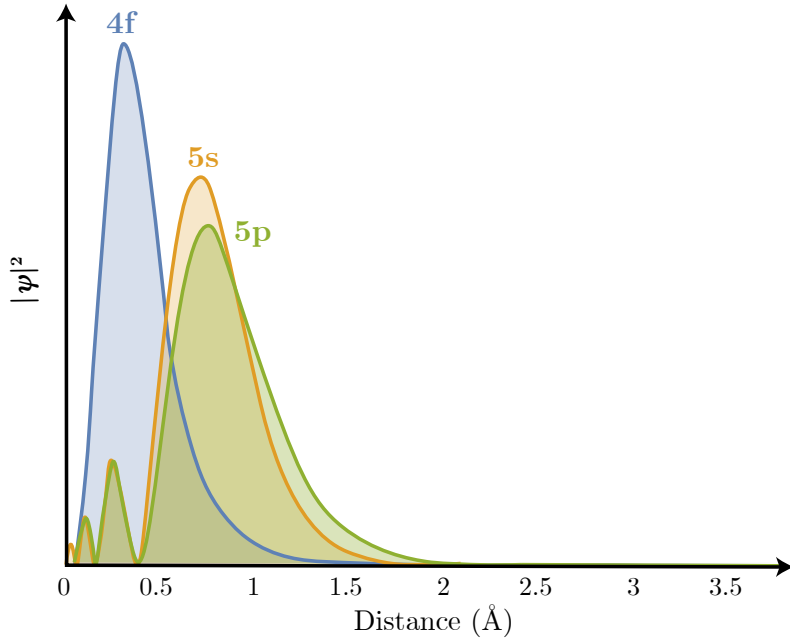


Figure 2.1: The radial electronic probability distribution of the rare earth gadolinium, showing that the valence electrons in the 4f shell are more likely to be found closer to the nucleus than the shielding 5s and 5p shells. Erbium has a similar probability distribution. Figure reproduced from [16].

2.1.2 Crystal structure

The crystal I am focussing on in this thesis is Y_2SiO_5 substitutionally doped with ^{167}Er at low concentrations (0.005%), which is known to have narrow linewidths [17], and long storage times at the 1550nm transition [6]. The low symmetry of this crystal structure means that the properties of the erbium atoms are anisotropic: they vary depending on orientation of the atom in the crystal. For this thesis I will be referring to the orientation of the crystal as D1, D2, and b (x, y, and z), as these are the principal axes of the refractive index tensor and are commonly used to designate orientations in Y_2SiO_5 . There are two sites of yttrium in the crystal unit cell, and as yttrium has a similar radius to erbium, there are therefore two sites for the erbium ions to substitute into. As these two sites have different surrounding atoms, the two sites for substituted erbium have slightly different energy levels and transitions [18]. The optical transitions in the 1550nm band of the two sites are 1536.14 nm for site 1 and 1538.57 nm for site 2 [19].

Although it is highly anisotropic, Y_2SiO_5 has one axis of C_2 symmetry, which points along the b axis. C_2 is a rotation symmetry, where a rotation of 180° is equivalent to the original position. This means that there are two orientations of erbium in each site with equivalent surrounding atoms. Without any applied fields the behaviour of these atoms is indistinguishable, however, their response to external fields are different, as I will discuss in the Hamiltonian section. In this work I am going to be focussing on both orientations of site 2, as it is site 2 that has shown the long coherence times needed for quantum memories.

2.1.3 Hamiltonian

Erbium has 68 electrons, including 11 in the 4f shell, so the energy level structure is complicated. As such, it is useful to break down the energy structure into contributions from different Hamiltonians. Rare earth crystals can be described by the following Hamiltonian [20]:

$$H = H_{FI} + H_{CF} + [H_{HF} + H_Q] + [H_Z + H_z]. \quad (2.1)$$

H_{FI} is the free ion term and defines the primary level structure of erbium without outside interactions. H_{CF} is the crystal field term from interactions between the ion and the crystal. H_{HF} and H_Q are the nuclear hyperfine interactions and quadrupole interactions, respectively. They form the hyperfine structure of a rare earth crystal. The next two terms vary depending on the crystal conditions, with H_Z representing the electronic Zeeman interaction, and H_z the nuclear Zeeman interaction [20]. External electric fields also influence the Hamiltonian, but I have not considered them here as they are not applied in my experiments. The overall contributions can be seen in Figure 2.2, and I will further describe these interactions in the following.

The basic energy level structure of erbium can be determined based on the free-ion term of the Hamiltonian (H_{FI}). A subsection of the free ion levels is shown in Figure 2.2) a). Of particular interest is the transition between $^4\text{I}_{15/2}$ and $^4\text{I}_{13/2}$ levels, as this is the lowest energy optical transition from the ground state and has a wavelength of 1538nm equivalent to approximately 194.9 THz. Transitions around this wavelength are in the low loss band for fibre optic cables.

The free ion levels of erbium split into more levels once placed into a crystal. This further splitting is because of the crystal field (H_{CF}), as shown in Figure 2.2) b). The crystal field is a fixed electric field because of charges in the crystal that lift the degeneracy in angular momentum (J) by an amount dependent on the erbium site symmetry. In $\text{Er}^{3+}:\text{Y}_2\text{SiO}_5$, this splits each energy level into $2J+1$ levels. As erbium has a half integer spin, it is a Kramer's ion and each energy level is doubly degenerate. In erbium the ground level has angular momentum $15/2$, so is split into eight doubly degenerate levels, and the excited $13/2$ level is split into 7 double degenerate levels. These splittings are on the order of 1-10 THz. Due to the crystal field interactions in $\text{Er}^{3+}:\text{Y}_2\text{SiO}_5$, m_J is not a good quantum number, so I will label the levels as Z_n for $^4\text{I}_{15/2}$, where n is 1 for the lowest energy level, and 8 for the highest. The crystal field levels of $^4\text{I}_{13/2}$ will be labelled the Y_n levels, with n going from 1 to 7. In this thesis, I will be focussing on exciting the optical transition between the $^4\text{I}_{15/2}(Z_1)$ and $^4\text{I}_{13/2}(Y_1)$ levels.

The hyperfine structure is a combination of the quadrupole (H_Q) and hyperfine interactions (H_{HF}), shown in Figure 2.2)c). The crystal field levels split into further levels because of interactions between the magnetic dipole moment of the nucleus and the electrons. Focussing just on the 1538nm transition of interest, as ^{167}Er has nuclear spin (I) of $7/2$, both the $^4\text{I}_{15/2}$ and $^4\text{I}_{13/2}$ levels are each split into 8 hyperfine levels on the order of 1 GHz for each of the possible nuclear spin quantum numbers ($m_I = |-7/2\rangle, |-5/2\rangle, \dots, |+7/2\rangle$).

Under the influence of a magnetic field there is a further perturbation on the hyperfine structure of the erbium - the Zeeman splitting, shown in Figure 2.2)d). The Zeeman splitting has two factors: the electronic Zeeman (H_Z), and the nuclear Zeeman (H_z). The

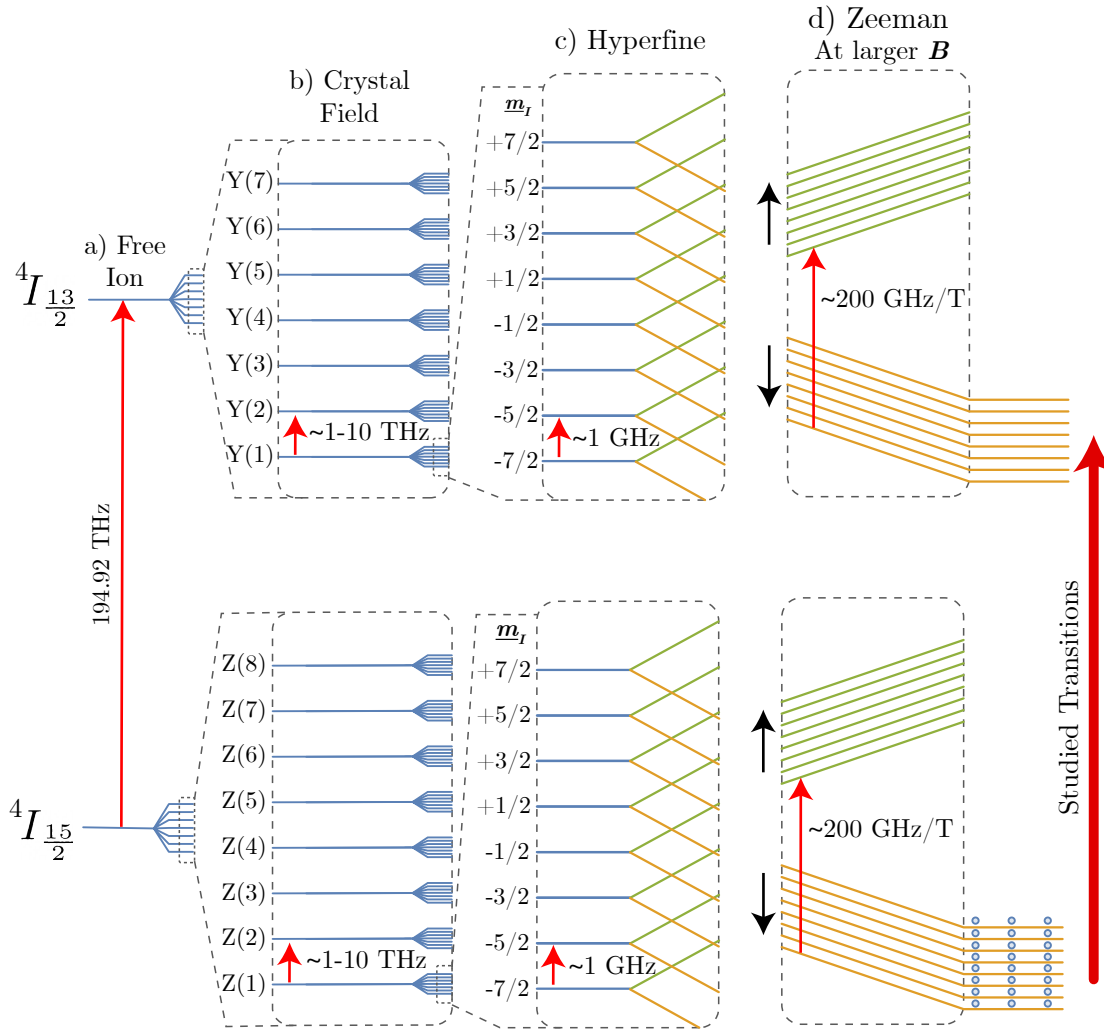


Figure 2.2: A breakdown of the $^{4}\text{I}_{15/2}$ to $^{4}\text{I}_{13/2}$ transition of erbium, focussing specifically on the studied transitions. The free ion term (H_{FI}) is shown in a). The crystal field term (H_{CF}) is shown in b). The hyperfine structure ($H_{HF} + H_Q$) is shown in c), with the initial Zeeman splitting of the doublets at small magnetic fields shown in green and yellow. The Zeeman splitting at larger fields (H_Z) is shown in d). At the low temperatures used in this thesis (below 2 K), the atoms occupy the hyperfine levels of the $^{4}\text{I}_{15/2}(Z_1, \downarrow)$ level. The transitions on the right of the diagram are those being studied in this thesis.

electronic Zeeman splitting is an interaction between the magnetic field and the dipole moment of the electronic (crystal field) state. It splits the doubly degenerate states, increasing the energy of one of the states, while decreasing the energy of the other by roughly 200 GHz/T for the ground states. The nuclear Zeeman is a smaller splitting due to the magnetic field interacting with the nuclear magnetic moment, however the order of the nuclear splitting is smaller than the electronic splitting by a factor of 1000, so can be ignored here.

Since the crystal is anisotropic, the electronic Zeeman splitting is dependent on the direction of the field. This dependence is described by the g-tensor:

$$H_Z = \mu_B (\vec{S} \cdot \vec{g} \cdot \vec{B}) \quad (2.2)$$

The Zeeman splitting is, therefore, almost entirely governed by the projection of this large g-value onto the magnetic field direction. The g-tensor is highly anisotropic and has only one large component, near the D1 axis in $\text{Er}^{3+}:\text{Y}_2\text{SiO}_5$. Recalling the axis of C2 symmetry along the *b* direction that relates the two orientations of the erbium site as described in section 2.1.2, the g-tensors for the two orientations have equal length but are pointing in different directions (see Figure 2.3). The result is that the two orientations will have the same splitting if the magnetic field is applied exactly along *b* or in the D1-D2 plane. If the field is pointed in other directions, the projection of the g-tensor onto the field direction will be different between the two orientations, and they will experience different Zeeman splittings.

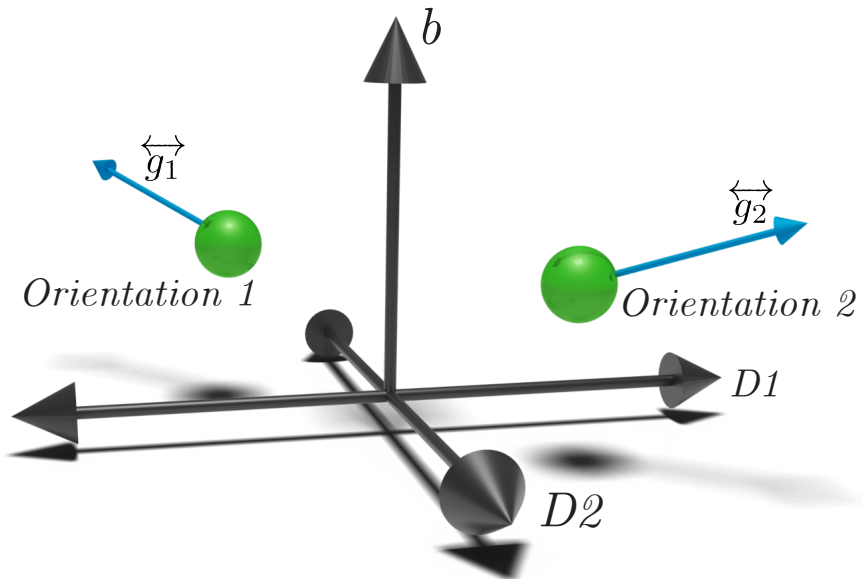


Figure 2.3: A diagram showing C2 symmetry around the *b* axis in Y_2SiO_5 , and the direction of their g-tensors. The dot product of the g-tensor with the magnetic field describes the level of Zeeman splitting. With a magnetic field applied along the *b* axis or D1-D2 plane, both orientations experience the same Zeeman splitting.

The exact energy level structure of the electronic ground ${}^4\text{I}_{15/2}(Z_1, \downarrow)$ and excited ${}^4\text{I}_{13/2}(Y_1, \downarrow)$ states at the magnetic field used in this project has been previously measured [6]. However, for my measurements I needed information about the structure of

the $^4I_{15/2}(Z_1, \uparrow)$ to $^4I_{15/2}(Z_1, \downarrow)$ transitions. These are difficult to measure at this high field as they are at frequencies greater than 1 GHz, so instead I used a simulation of the energy level structure based on crystal field modelling software (PYCF). This model was developed by Mike Reid and Sebastian Horvath, and uses the above Hamiltonian with a large number of fitted parameters that are input depending on the material [21]. I use the parameter fit to $\text{Er}^{3+}:\text{Y}_2\text{SiO}_5$ in [22]. Thus, I was able to calculate the energy level structure for the magnetic field used in these experiments. Although the determined splittings do not exactly match measured values (a common problem with crystal field models of low symmetry crystals like $\text{Er}^{3+}:\text{Y}_2\text{SiO}_5$), they give a good approximation of the trends that will be seen.

2.1.4 Hyperfine transitions

The above discussion explains the general behaviour of the optical $^4I_{15/2}(Z_1, \downarrow)$ to $^4I_{13/2}(Y_1, \downarrow)$ transition. Each of these levels has eight hyperfine states contributing, and transitions between the ground and excited hyperfine states determine the structure of the optical transition. All measurements in this thesis were performed at magnetic fields of 7 T along the D1 axis, and at temperatures below 2 K. Under these conditions, there are three main groups of transitions between the hyperfine levels and are shown in Figure 2.4(a). The strongest optical transitions are the 8 excitations that do not change the nuclear spin projection between the ground and excited states. I will refer to these as the $\Delta m_I = 0$ transitions. Weaker transitions that change the nuclear spin are observable with $\Delta m_I = \pm 1$ because the crystal does not have strong selection rules. Changes in nuclear spin larger than 1 can occur, however, are much weaker. The experimental spectrum of these transitions is shown in Figure 2.4(b). Although the hyperfine levels are equally populated, the peaks are not necessarily symmetric, as the transitions between the different hyperfine levels have different probabilities of occurring.

2.2 Storing Quantum Information

A quantum memory needs to encode a quantum state onto a material and at a later time retrieve the same state. A useful material to use is an ensemble of atoms, as they are highly absorbing of inputs because of the large number of ions. The quantum state to be stored is encoded as a pulse of light and sent into the ensemble where it is absorbed by the atoms. This excites the ensemble into a well-defined superposition state that matches the input. When the state needs to be retrieved a process is applied that results in a time reversal of the absorption process, causing the ensemble to re-emit the absorbed light. There are various methods to reverse the time evolution of the ensemble state, known as different memory protocols. There are a few key concepts that are necessary for understanding a simple quantum memory protocol. In the following I discuss these concepts and describe a common quantum memory protocol - the atomic frequency comb.

2.2.1 Two-level Systems and the Bloch Sphere

In quantum computing, information is stored as qubits. These are different than a classical bit (either 0 or 1), as qubits are a superposition of two states, $|0\rangle$ and $|1\rangle$. In rare-earth quantum memories, this is typically achieved by using an ensemble of atoms with two energy states, such as ground and excited energy levels, or spin up and spin down. For

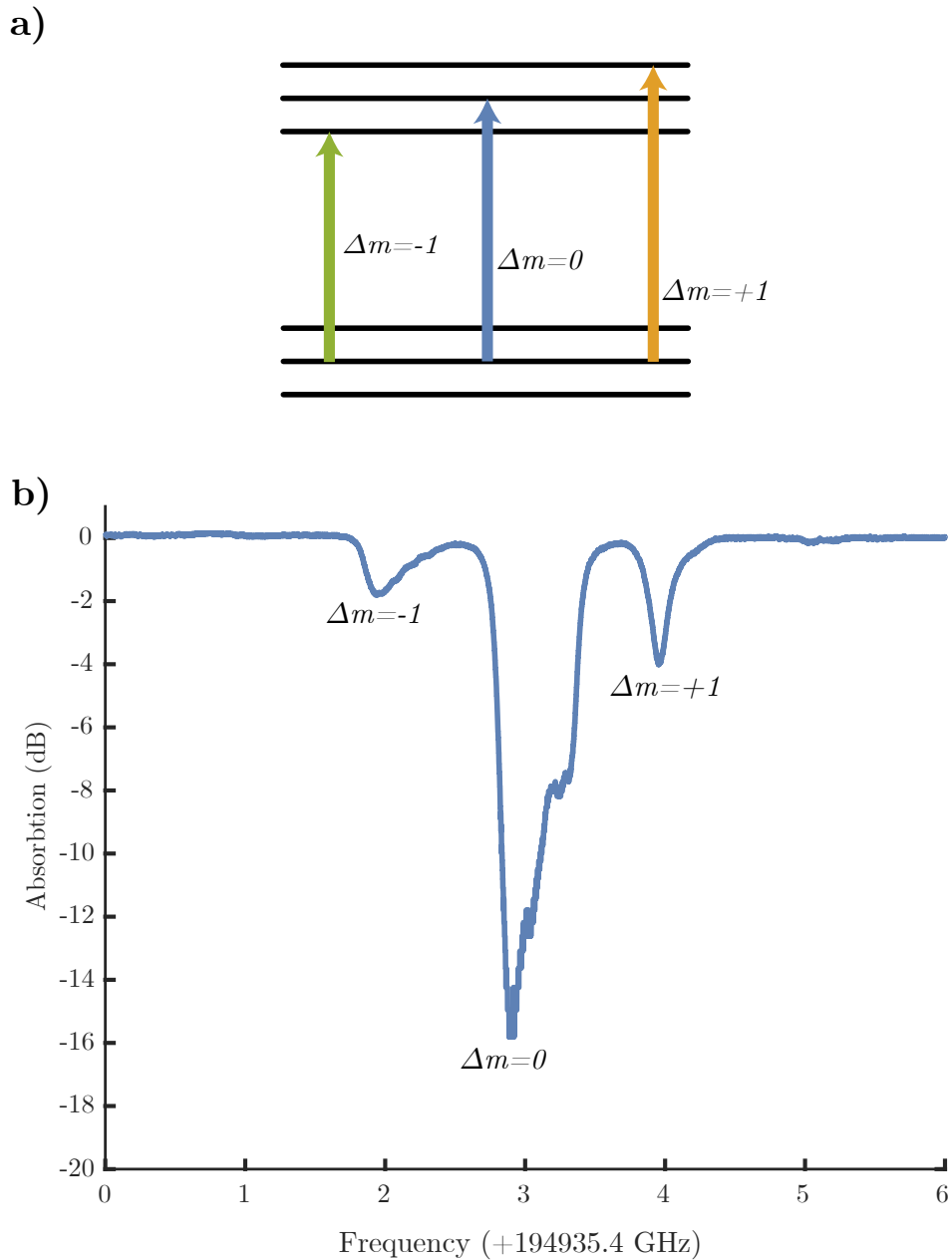


Figure 2.4: The different types of transitions are shown in a), with the blue transitions changing the spin projection by 0 ($\Delta m = 0$), the orange transitions changing the spin projection by +1 ($\Delta m = +1$), and the green transitions changing the spin projection by -1 ($\Delta m = -1$). The resulting absorption spectrum of $\text{Er}^{3+}:\text{Y}_2\text{SiO}_5$ site 2 at 1.7 K and 7 T applied field is shown in b). The transitions are not symmetric, as different transitions have different probabilities and frequency separation.

$\text{Er}^{3+}:\text{Y}_2\text{SiO}_5$, information would be stored as a superposition of $^4\text{I}_{15/2}(Z_1)$ and $^4\text{I}_{13/2}(Y_1)$ energy levels. A general qubit is of the form:

$$|\psi\rangle = \cos \frac{\theta}{2} |0\rangle + e^{i\phi} \sin \frac{\theta}{2} |1\rangle. \quad (2.3)$$

This two-angle description can be conveniently represented geometrically by using a vector pointing from the origin to a point on the surface of a sphere, as devised by Felix Bloch [23] (refer to Figure 2.5). In the Bloch sphere description of a two-level atom, the lower pole of the sphere represents the ground state, and the upper pole the excited state. Points in between are all the superpositions of these states. When unperturbed, the state evolution can be visualised as the vectors precessing laterally around the sphere at their transition's frequencies (variations of ϕ), while maintaining the probability of measuring either state (governed by θ). This is a description of the Bloch sphere for a single atom, however, Bloch spheres can also be used to describe ensembles of atoms. In this case, we can plot multiple vectors onto the Bloch sphere. The state of the ensemble can then be considered as the mean of the individual vectors.

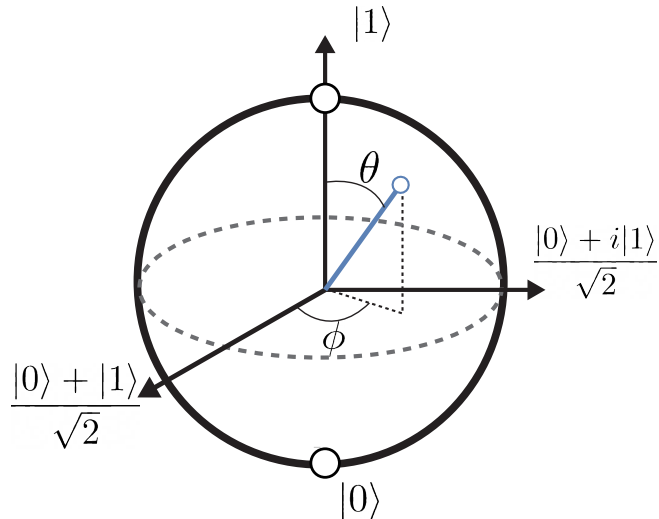


Figure 2.5: A visual representation of the Bloch sphere. A vector pointing down describes an atom being in the ground state, a vector pointing up describes an atom in the excited state, and anything in between is a superposition state.

There are three important time scales for quantum information storage considerations. The first is the lifetime of an excited state (T_1). This can be thought of the time that governs an atom in the excited state (at the top pole) falling to the ground state (the bottom pole). The next time scale to be considered is the coherence time (T_2). This describes how long the phase of the superposition state (ϕ) is well-defined. The final time scale is the dephasing time and is described in the following paragraph.

Individual atoms have a linewidth dictated by the coherence time, called the homogeneous broadening ($1/(\pi T_2)$), and is as shown in Figure 2.6(a). Ensembles of ions can have much larger linewidths because of the frequencies of individual atoms. In a material, the frequencies of individual atoms will shift because of different interactions due to imperfections

in the crystalline environment. Although each atom will maintain its same homogeneous broadening, they will be centred around different frequencies, and the overall linewidths of the ensemble is much larger - it is inhomogeneously broadened (shown in Figure 2.6(b)). Typically, the inhomogeneous broadening is on the order of 10^4 (but can be up to 10^7) times greater than the homogeneous broadening [24]. If an ensemble of atoms is put into a superposition state, each atom will evolve according to its own specific frequency, and the state of the ensemble will be lost, on a timescale given by the inhomogeneous broadening. This is the dephasing time. For example, imagine an inhomogeneously broadened ensemble of atoms that all start on the equator of the Bloch sphere along the x axis. Over time, the atoms would dephase, and the ensemble vector would be pulled to the centre of the Bloch sphere, and from the point of view of any measurement of the atoms, they would appear to have decohered. However, because the inhomogeneity in frequency is constant over time, methods exist to remove the dephasing it causes, such as the photon echo described in the next section.

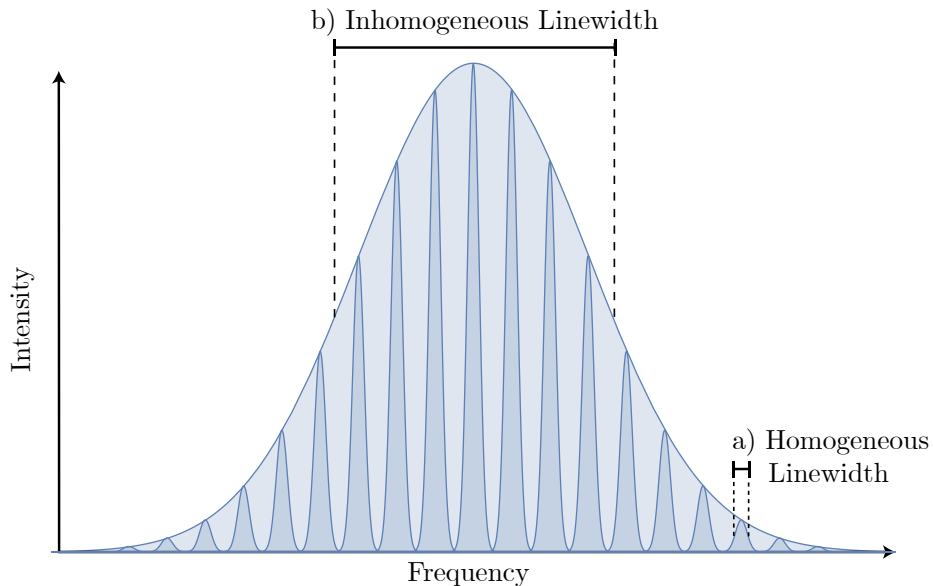


Figure 2.6: A comparison between homogeneous and inhomogeneous broadening. The homogeneous linewidth is shown in a) and is the natural linewidth of the atoms. The inhomogeneous linewidth is shown in b) and is the combination of many atoms with shifted frequencies.

2.2.2 Photon echoes

The simplest quantum memory protocol is a photon echo, and this demonstrates many of the principles used by other protocols. This is best described by considering an inhomogeneously broadened ensemble of atoms as many vectors on the Bloch sphere (see Figure 2.7(a)). The ensemble of atoms starts off in the ground state, with each of the vectors pointing directly down. A pulse of light is then applied to the atoms, exciting them to a 50% superposition of the two states $\left(\frac{1}{\sqrt{2}}|0\rangle + \frac{1}{\sqrt{2}}|1\rangle\right)$. This pulse of light is called a $\pi/2$ pulse as it rotates the vectors up the Bloch sphere by $\pi/2$ radians. The superposition states of these atoms will evolve over time, rotating around the Bloch sphere at different rates because of their different detuning from the light frequency, as governed by the de-

phasing time. After a time delay (τ), the aim is to reverse the dephasing, and this can be achieved by rotating all the atoms π radians around the horizontal axis by applying a π pulse. Each of the atoms will continue to evolve at the same rate, but now in the opposite direction. After the time τ , all the atoms will be in phase and they collectively emit a photon echo related to the input state. The input sequence and result can be seen in Figure 2.7(b). Although a photon echo is a method of storing a quantum state, it does not make for a good quantum memory as it amplifies the signal, introducing noise [25, 26].

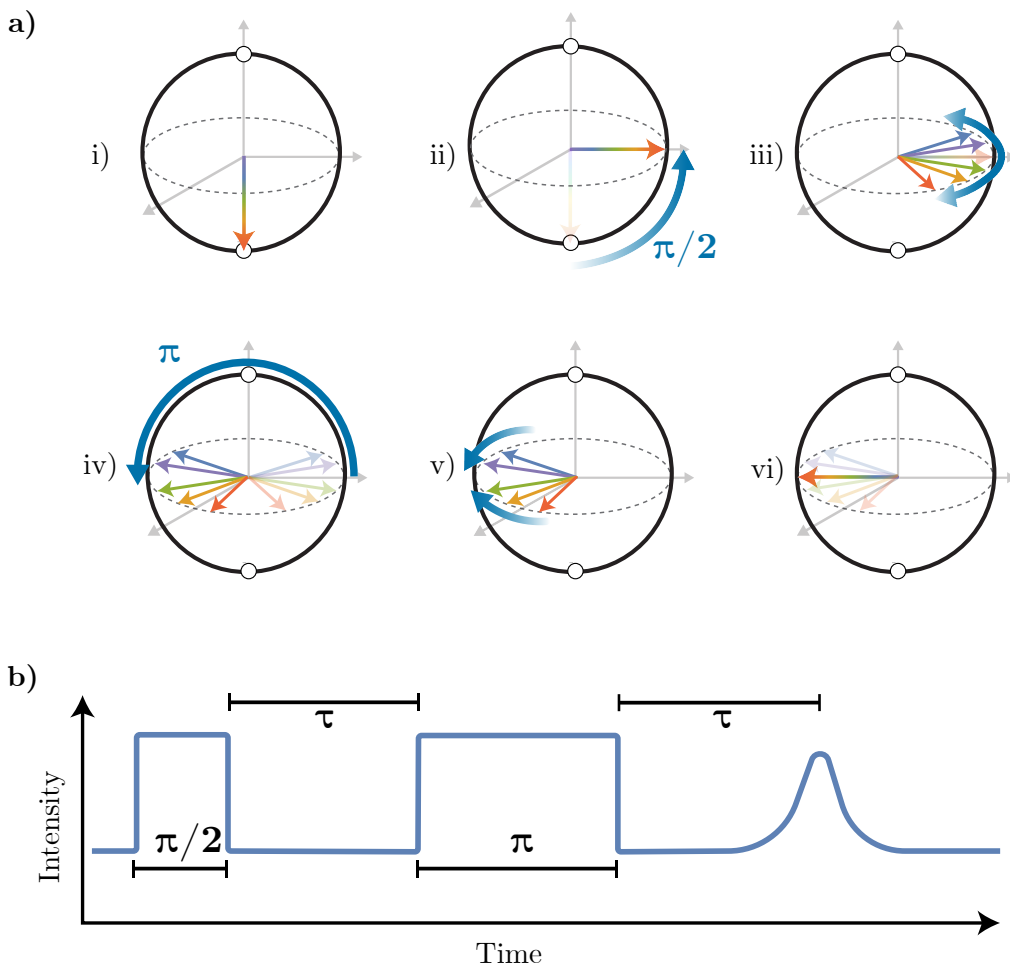


Figure 2.7: The overall photon echo sequence is shown in a). In i), all atoms are in the ground state. In ii), a $\pi/2$ pulse has been applied that moves all the atoms to a superposition state. In iii), the atoms dephase around the equator of the Bloch sphere, governed by their own individual detuning. After time τ , a π pulse is applied rotating all the atoms around the equator of the Bloch sphere, as shown in iv). The atoms then continue to evolve at the same rate as before, as shown in v). These then rephase, as shown in vi). The inputs and echo are shown in b).

Photon echoes can be used to measure the coherence time because they remove the effect of inhomogeneous broadening [27, 28]. This is done by taking multiple measurements of the echo intensity with different delays between the $\pi/2$ and π pulses. For short delays, the intensity of the photon echo will be greatest, with all the atoms rephasing at the same time at the same superposition. Over time, as the atoms lose coherence, there will be a

reduction of the echo intensity. This intensity follows an exponential of the form $e^{-2\tau/T_2}$ (refer to Figure 2.8). As such, the coherence time can be extracted as the time where the echo intensity is $\frac{1}{e}$ of the zero delay intensity. I will discuss some interactions that affect coherence times in Section 2.3.

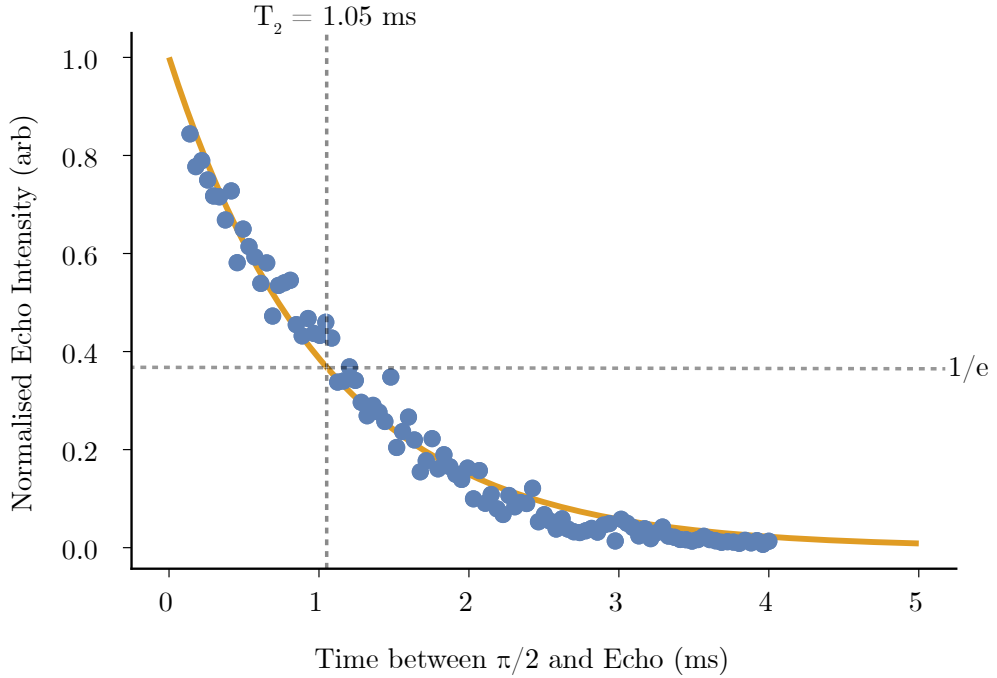


Figure 2.8: A measurement of coherence time using photon echoes. The data has been normalised, and a curve has been fit to the data. The coherence time is when the echo intensity is $1/e$, and in this measurement is $T_2 = 1.05$ ms.

2.2.3 Spectral preparation

Different quantum memory protocols require the inhomogeneously broadened ensemble to be spectrally prepared to impose a particular frequency profile on the atoms. This is primarily performed by a process called hole burning. Hole burning involved exciting a particular range of atoms by using a laser with matching frequency, as shown in Figure 2.9(a)i). These atoms will be excited to a higher energy level, typically with the same spin projection, that they will eventually decay from at a rate given by the state lifetime. Although the atoms will typically decay back to the ground level with matching spin projection, there is a small probability the atom will decay to another spin projection, as shown in Figure 2.9(a)ii). By continually exciting this transition, all the atoms at the resonant frequency will eventually decay to a different level, and the laser will not interact with any atoms. This causes a hole to form in the inhomogeneous broadening, as shown in Figure 2.9(b)). The hole-burnt atoms will have been moved into other levels in the system.

2.2.4 The atomic frequency comb protocol

A common quantum memory protocol that makes use of spectral preparation and shows the fundamental steps of quantum memories is the atomic frequency comb (AFC). An AFC

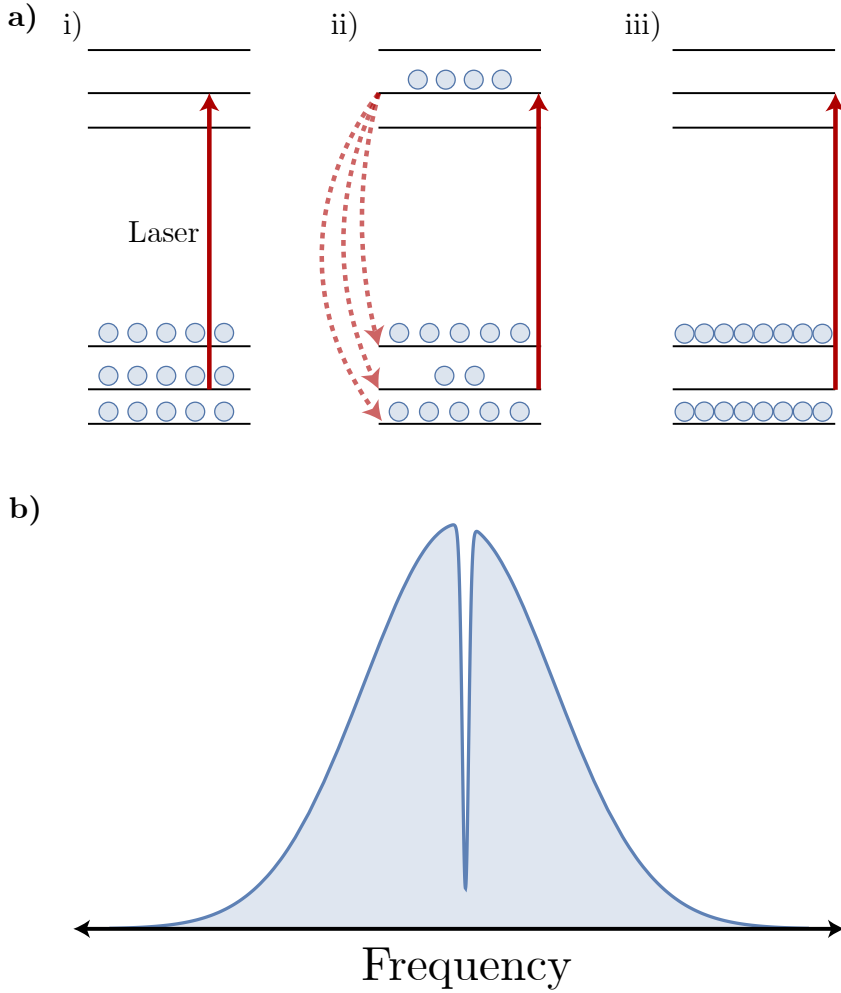


Figure 2.9: The hole burning process is shown in Figure a). In i), the laser excited atoms up to the excited state. The atoms will then fall back to the ground state, with some atoms changing spin projection as they fall, as shown in ii). After some time, all the atoms will have fallen to non-resonant levels, as shown in iii). The resulting spectrum is shown in b).

starts with an inhomogeneously broadened set of atoms, which are spectrally prepared by burning holes at regular intervals. This leaves a ‘comb’ shape in the optical frequency profile of the ensemble (see Figure 2.10(a)). Light is then input that can be absorbed by resonant atoms in the comb. To ensure that the ensemble fully absorbs all photons, the bandwidth of the pulse must be greater than the separation between the peaks. In the limit of a perfect comb, each peak in the comb can be thought of as a delta function in frequency, so the excited ensemble of atoms contains only atoms at a fixed set of evenly-spaced frequencies separated by Δ . Thus, as the excited atoms evolve (similar to in the photon echo), they will rephase a time $2\pi/\Delta$ later, as shown in Figure 2.10(b). The width of the teeth (γ) changes the number of absorbing atoms, and needs to be chosen carefully to absorb the input frequencies fully while maintaining a comb shape.

This type of AFC is known as an optical delay line - it delays the quantum state by a fixed amount determined by the comb frequency spacing. The AFC can also be operated as a quantum memory where the state can be recalled on demand. To do this, another

light pulse is applied to transfer the state from the optical transition to a ground state spin transition during the dephasing time. The state is maintained on the spin transition until another pulse transfers the state back to the optical transition [10]. The maximum experimentally demonstrated efficiency in an AFC so far is 58% [29].

AFCs are considered to be the quantum memory protocol with best multiplexing capability [29], and can be multiplexed using the three methods discussed in Chapter 1. Frequency multiplexing involves inputting different frequencies or defining combs at multiple frequencies. This allows for the excitation of different atoms in the comb that rephase at the same time [30, 31]. Temporal multiplexing is achieved by inputting the states at different times [32]. The modes will then rephase in the input order. Spatial multiplexing is achieved by using multiple laser beams to define AFCs in different parts of the crystal.

With the exception of spatial multiplexing, the increased density of excited atoms when multiplexing is expected to lower the efficiency. This is because as more states are stored over the same number of atoms, the efficiencies are degraded as there are less atoms for each quantum memory. Furthermore, with higher excitation density, the interaction strength between atoms is increased, degrading the quantum information being stored. Less well studied are long range interactions in rare-earth crystals, and how they will limit the multiplexing capacity. It is expected that any long-range interactions would affect all three multiplexing methods.

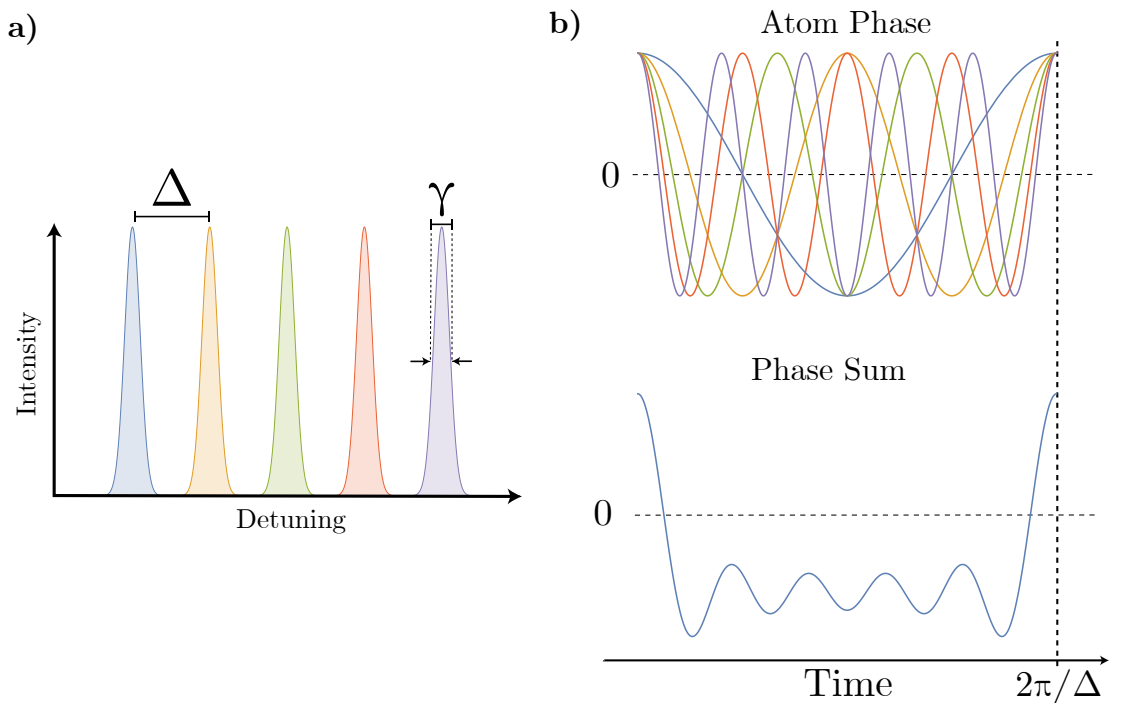


Figure 2.10: The spectrum after spectral preparation for an AFC is shown in a). Δ is the frequency splitting between the comb teeth, and γ is the width of the comb teeth. The rephasing process is shown in b). At a time $2\pi/\Delta$, all the atoms will align in phase, collectively emitting the input state.

2.3 Interactions that effect quantum information storage

In this thesis, I will investigate interactions that could affect quantum memories in $\text{Er}^{3+}:\text{Y}_2\text{SiO}_5$. In particular, I studied the effects of interactions on the spectral hole-burning dynamics in this material. Nearly all quantum memory protocols require spectral preparation via spectral hole-burning, and the memory performance (such as the efficiency for the case of the AFC) is dependent on the quality of this spectral preparation. Interactions can also directly affect the coherence time, and I briefly studied this effect. In this section, I describe the interactions that can affect spectral hole lifetimes and coherence times, and outline how these could affect quantum memories.

The lifetime of a spectral hole is limited by the lifetime of the hyperfine levels that the atoms are transferred to by the hole-burning process. As atoms start to move back into a hole-burnt level, the spectral hole fills in. Similar to any other energy level in a solid, three processes can limit the lifetime of hyperfine states: radiative decay, non-radiative decay, and direct ion-ion interactions. Radiative decay is negligible at the low frequencies of hyperfine transitions (GHz), so is not being considered.

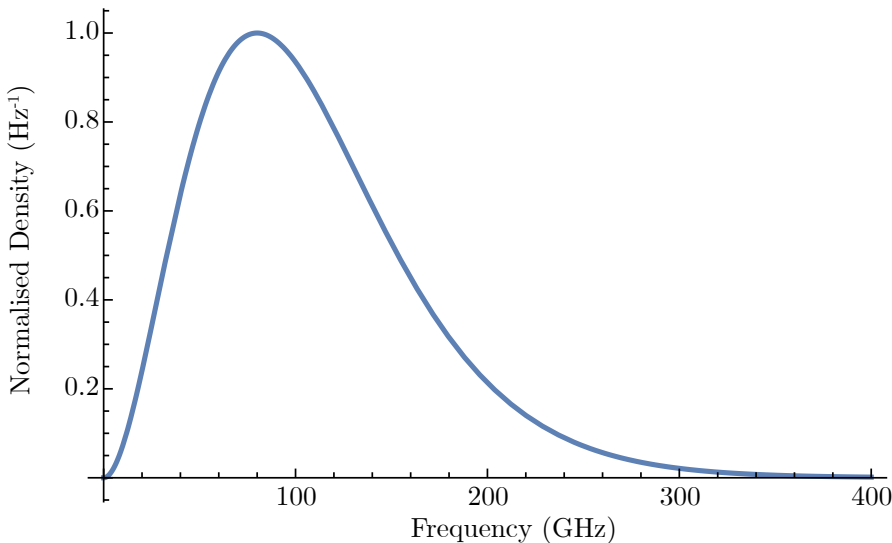


Figure 2.11: A plot of the phonon distribution at 1.7 K. The peak number of phonons at this temperature is 80 GHz.

Non-radiative decay, or spin-lattice relaxation, occurs via the exchange of energy between the ions and vibrations of the lattice (phonons). The spin-lattice relaxation rate is determined by the coupling strength between the ions and the phonons, the density of empty phonon modes at that frequency, and the density of phonons resonant with the transition (determined by the crystal temperature). The density of phonons as a function of frequency follows the thermal distribution, a plot of which is shown in Figure 2.11. The number of phonons peaks at around 100 GHz when the crystal is at 1.7 K. One way of mitigating the effect of these phonons, used in this project, is to apply a large magnetic field to the crystal that increases the splitting between energy levels, so that there are few phonons resonant with the atoms. At the 7 T field used in this work, the lowest electronic energy level splitting is 1500 GHz, far from the peak of the thermal phonon distribution

There are three main processes by which phonons can interact with rare earth ions in crystals [33]. A general expression of phonon induced relaxation with temperature is:

$$\gamma(T) = \gamma_d T + \gamma_r T^9 + Y_{or} f^3 \exp\left(-\frac{hf}{kT}\right). \quad (2.4)$$

The first relaxation (γ_d) is a direct transition, where the energy of the phonon matches that of the transition. The second (γ_r) is a Raman process, where a phonon excites an atom to a virtual energy state, and a second phonon is emitted, lowering the energy of the atom to a non-virtual energy state. The third process, Orbach coupling (γ_{or}), is a two phonon process like the Raman process, however the atom is excited to an intermediate higher energy state, rather than a virtual state. At very low temperatures, the two multiphonon processes are reduced significantly due to the lack of high energy phonons, and phonon relaxation is mostly attributed to the direct transition process, which itself can be substantially suppressed by applying magnetic fields as described above.

Optical excitation will induce phonons that do not conform to the thermal distribution (see Figure 2.12). These come from excited atoms lowering in energy and emitting a range of non-equilibrium phonons. Overtime, these phonons will thermalise, heating up the crystal. As the crystal heats up, the number of phonons will increase, and the thermal distribution will shift. If the crystal heats up significantly, the thermal distribution can be shifted enough to have equilibrium phonons resonant with the transitions of atoms (shown by the orange curve). Spectral holes burned at frequencies far from the peak of the phonon distribution will then be more likely to be filled by atoms excited by the equilibrium phonons.

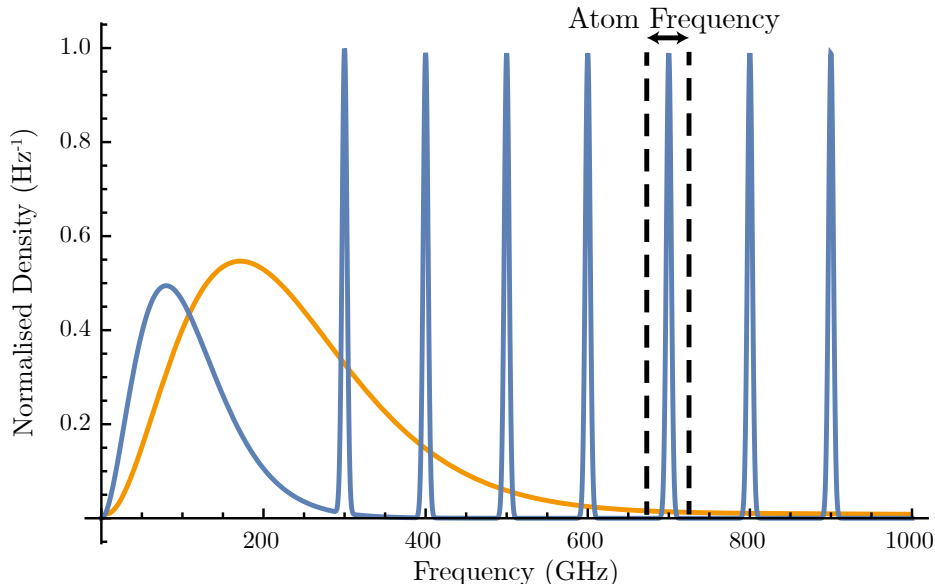


Figure 2.12: A plot of a typical phonon distribution (blue line) if non-equilibrium phonons are present, shown by the sharp spikes. If the non-equilibrium phonons are resonant with an atom's frequency, then they can excite that atom. The other phonons will be absorbed into the thermal distribution, raising the temperature of the crystal. If the temperature is sufficiently raised (orange line), the thermal distribution of phonons will shift enough to generate equilibrium phonons that are resonant with the atom's frequency.

Another concern is if any of the non-equilibrium phonons are already at frequencies resonant with transitions. These phonons would excite those transitions, and the atom will then relax, potentially falling to a level different than the one it came from. This would also fill in a spectral hole. This effect is enhanced if the absorbed phonon is re-emitted and the process is repeated. It will only end when the non-equilibrium phonon is scattered into the thermal distribution. If the phonon falls back to the same hyperfine level, this will not fill the spectral hole, however, will change the phase of the atom. This would affect a coherence measurement made using photon echoes.

If non-equilibrium phonons are resonant in $\text{Er}^{3+}:\text{Y}_2\text{SiO}_5$, they are most likely to come from only a few energy levels. The phonons are produced as optically excited atoms fall back down to the ground state, and are going to be from direct transitions, as two phonon processes are small under the low temperature conditions. These transitions must be to the ground state, because otherwise the phonons produced would be non-resonant with, and thus, not able to re-excite the ground state atoms to fill in the hole. The lifetimes of the phonons are related to their frequency ($T_1 \propto f^{-5}$), with high frequency phonons having short lifetimes as they scatter rapidly into the thermal distribution, making the phonons more likely to be of a lower frequency. Combining these points, the phonons will most likely be transitions from low energy electronic states to the ground state. Note that they will not be the lowest-energy group of phonons (from hyperfine transitions within the ground state) because these states have long lifetimes (minutes) and therefore very weak coupling to phonons. This means the phonons are most likely to come from the $^4\text{I}_{15/2}(Z_1, \uparrow)$ state, although could also be from the $^4\text{I}_{15/2}(Z_2, \downarrow)$ state.

Non-equilibrium phonon research in rare-earth crystals has been primarily focused on praseodymium doped crystals, starting in the 1980s [34]. This is because praseodymium has an energy structure where the resonant phonons are at a much lower energy, and much longer lived [24]. Non-equilibrium phonons generated by a powerful perturbation beam were observed to be the primary cause of lower storage times in $\text{Pr}^{3+}:\text{YAlO}_3$ [35], and storage limitations in $\text{Pr}^{3+}:\text{Y}_2\text{SiO}_5$ were partially attributed to phonons, although they could not be fully distinguished from short range decoherence [36].

Non-equilibrium phonons have been observed in $\text{Er}^{3+}:\text{Y}_2\text{SiO}_5$, in experiments at mK temperatures and fields below 10 mT. There, the phonons had lifetimes of 0.3 ms [37]. However, these results are not directly applicable to the regime studied here because both the resonant phonon frequency and the coupling strength to the spins changes with field. Outside of this low temperature, low field regime, it is not well known how significantly phonons contribute to lowering the storage times in $\text{Er}^{3+}:\text{Y}_2\text{SiO}_5$, with more phonon properties needing to be measured [38].

The final interaction that can affect hole lifetimes is ion-ion interactions in the form of hyperfine cross relaxation, or spin-spin interactions. This is where nearby ions in two different energy levels exchange energy. Hyperfine cross relaxation is a magnetic dipole-dipole interaction, and its rate is determined by the size of the magnetic moment and the density of ions in the crystal. At low temperatures, cross relaxation can dominate the hyperfine lifetime even in low concentration crystals, like the 0.005% $^{167}\text{Er}:\text{Y}_2\text{SiO}_5$ crystal studied here. For a spectral hole, spin-spin cross relaxation can cause the hole to fill in if an atom in the ensemble exchanges spin with one outside of the ensemble. The hole can also be broadened by spin exchanges between atoms outside the ensemble (e.g. if the other atom has a different optical frequency to the atom in the hole), as this changes

the surrounding environment, spreading the frequencies (spectral diffusion). Although spectral diffusion changes the width of the hole, the total number of atoms in the hole would remain the same.

Spin-spin cross relaxation is a significant cause of reduced lifetimes in $\text{Er}^{3+}:\text{Y}_2\text{SiO}_5$, as erbium ensembles have large electron spins giving large magnetic spin moments. However, as spin flip-flops require atoms in the other state to flip-flop with, they can be decreased by spin-polarising the material. As described earlier, with a large magnetic field applied the electron spin splitting is large, and there are few phonons available to excite atoms into this level, thus the material is spin polarised with all atoms in the lowest electronic state. A 7T field along the D1 axis increases hole lifetimes to 1 minute, hyperfine lifetimes to 12 minutes [39], and optical coherence times to 4.38 ms [40]. The hole lifetimes are shorter than the hyperfine, as the hole is filled by the spin-spin cross relaxation, and the hyperfine lifetime is only from spin-lattice effects. All experiments in this thesis are performed using the same 7 T field applied along the D1 axis, so the effects of spin-spin cross relaxation are reduced.

2.4 Chapter summary

In this chapter I provided the background information and motivations behind the studies in this thesis. I discussed the properties of $\text{Er}^{3+}:\text{Y}_2\text{SiO}_5$, showing why its electronic structure gives long coherence times at telecommunication frequencies. I then discussed the transitions relevant to this thesis - the ${}^4\text{I}_{15/2}(Z_1,\downarrow)$ to ${}^4\text{I}_{13/2}(Y_1,\downarrow)$ transition, and the spectra resulting from the hyperfine structure of these levels. I also discussed the crystal structure, focussing on the two orientations of erbium in the crystal, and its anisotropy in response to a magnetic field. The symmetry of these two orientations will be utilised in part of the experimental design. I then covered quantum information, and a basic quantum memory protocol, showing where information loss can occur. Finally I went through the relevant interactions that affect the information storing ions. The following chapters in this thesis are studies of these interactions, determining which are occurring and then determining their properties.

Experimental Methods

In this chapter I will describe the experimental setup used for all of my experiments. I will start with the dimensions and features of the cryostat used in experiments, and the resulting design of the sample rod and mount. I will then discuss the motivation and layout of the laser setup used for the experiments. Finally, I will describe the technique used to measure the magnitude of the perturbation on the atoms. Then I will derive the equation used to determine the effect on the atoms.

3.1 Sample rod design

The experiment was designed around the dimensions and layout of the cryostat which was necessary to reduce the temperature of the sample. The cryostat used in experiments maintained temperatures of approximately 1.7 K. Inside the cryostat is a tall sample space, with a 15 T magnet surrounding the bottom. The magnet has a bore of 30 mm and applies a field of 7 T within the sample space in the vertical direction. There is a window located underneath this area, where signals can be input to the sample and reflected out with a mirror behind the sample. These constraints needed to be considered when designing the sample rod.

The most important part of the sample rod design was being able to rotate the crystal, as I planned on utilising the anisotropy of the two orientations of atoms to create a controllable frequency separation between the atoms. With a fixed magnetic field, rotating the crystal is equivalent to changing the direction of the applied field. To make the rotations, I used a two-axis set of piezoelectric goniometers from Attocube, as they were available from a previous project. Each goniometer has ± 3 degrees of travel, and is highly adjustable, with the ability to make small angle adjustments under extreme conditions (like large magnetic fields, lower pressures, and low temperatures), while maintaining a common centre point.

With the ability to rotate the crystal, I wanted to ensure that the optimal orientation and rotation axis was chosen, as I needed to maximise the frequency range from rotation. The D1 axis of the crystal needs to be along the same axis as the magnetic field in the cryostat, so it was positioned along the z direction, and I aligned the D2 and b axes of rotation with the Attocube axes of rotation. To simplify experiments, I wanted to only have to rotate the sample around one of the axes. To determine the best rotation axis, I used the crystal field modelling with an applied field of 7 T rotating ± 3 degrees around either axis, as shown in Figure 3.1. These simulations returned similar differences between the ground state

transition frequencies I wanted to tune, at approximately 16 GHz. However, rotations around the D2 axis would shift the optical transition frequencies by a larger amount, and it was this optical frequency I used to determine the angle the Attocube had moved. As such, I chose to only rotate the sample around the D2 axis during measurements.

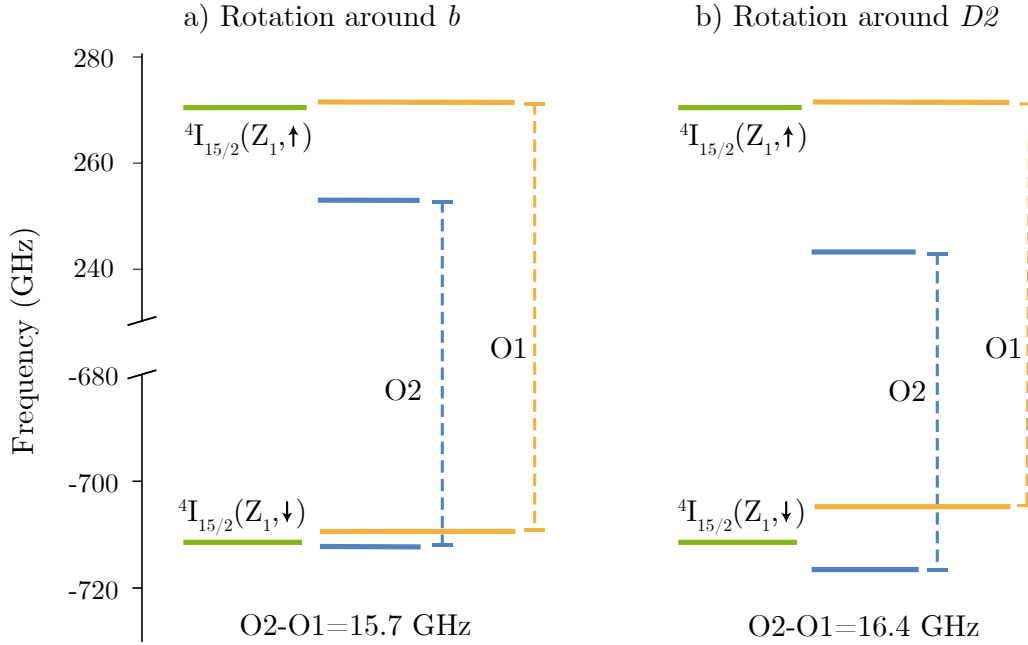


Figure 3.1: Shifts in the electronic levels after rotating 3 degrees around a) the D2 axis, and b) the b axis. Orange levels are the shifts of orientation 1 (displayed as O1), while the blue levels are the shifts in orientation 2 (displayed as O2). Rotation around the D2 axis gives a larger frequency difference between the two orientations, so I used this as the rotation axis for experiments.

With the rotation mechanism and the orientation of the crystal determined, the sample mount needed to be designed. The sample chosen was a $3 \times 3 \times 10$ mm 0.005% $^{167}\text{Er:Y}_2\text{SiO}_5$ crystal. I designed a mount for the crystal and mirror as shown in Figure 3.2. The crystal needed to be held by a mount that would fit within the 30 mm bore of the magnet and accommodate a mirror to reflect the input light out of the cryostat. This mirror was mounted separately from the sample to ensure that it was not rotated and would consistently reflect the laser beam back into the detection optics. As the input window is at the bottom of the cryostat, I placed this mount upside-down so beams could enter the crystal. Underneath the crystal there is a channel for light inputs to pass through and reflect off the mirror. I mounted these pieces to the end of a long carbon fibre sample rod available from previous experiments that positioned the setup at the bottom of the cryostat.

3.1.1 Experimental Setup

The basic experimental setup is shown in Figure 3.3. The optical setup of the experiment was a modified version of a PhD student's experiment, where an additional beam path was sent into the crystal. Thus, I will concentrate on those parts of the setup relevant for my work. The first path was the probing path, and used to burn holes, perform photon echo sequences, and for taking spectra. The second path was for perturbing the system

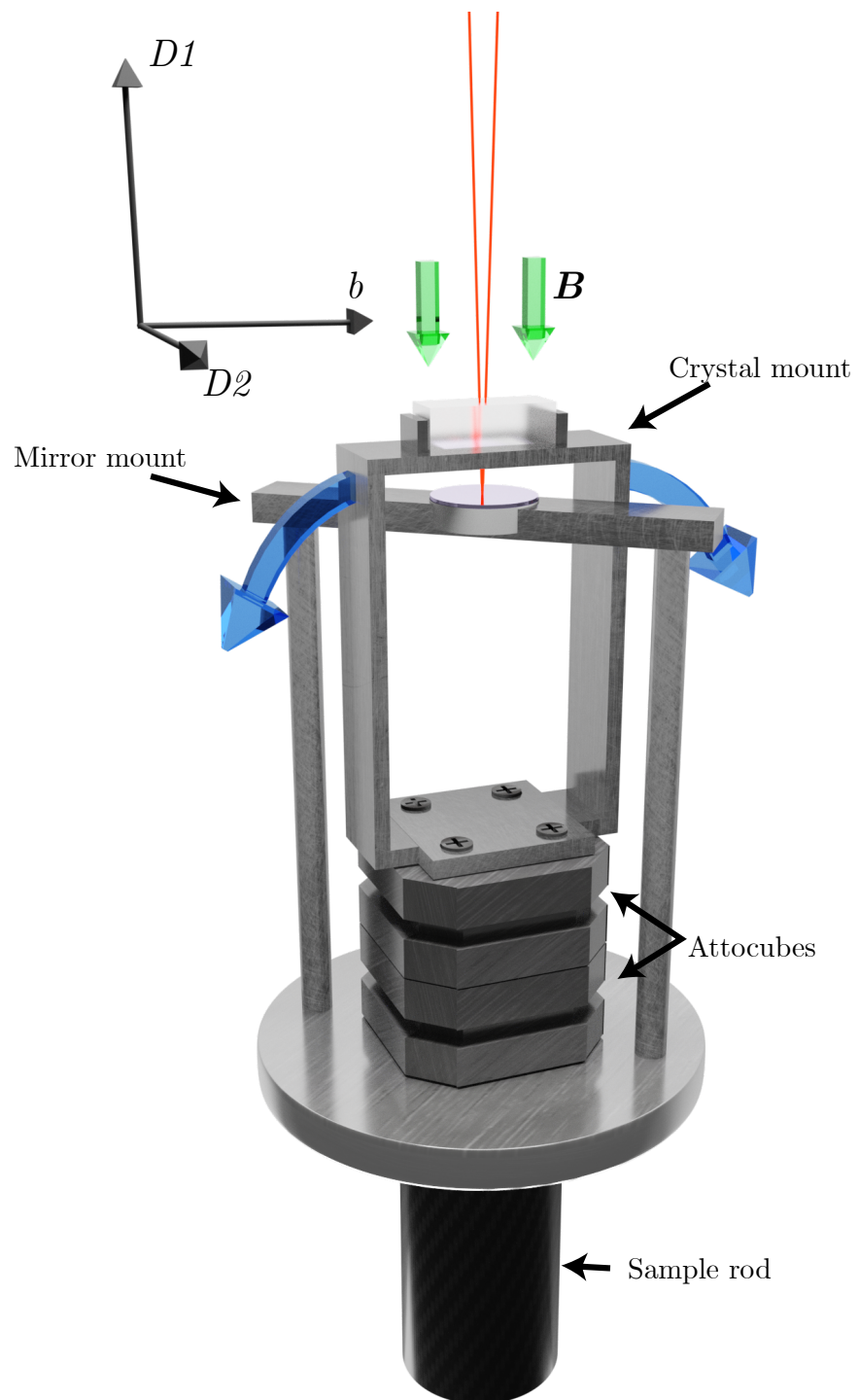


Figure 3.2: Render of the crystal and mirror mount design. The crystal mount is attached to the Attocubes, placing the crystal 40mm above the axis of rotation. The mirror mount is fixed to the sample rod to maintain the position of the mirror underneath the crystal.

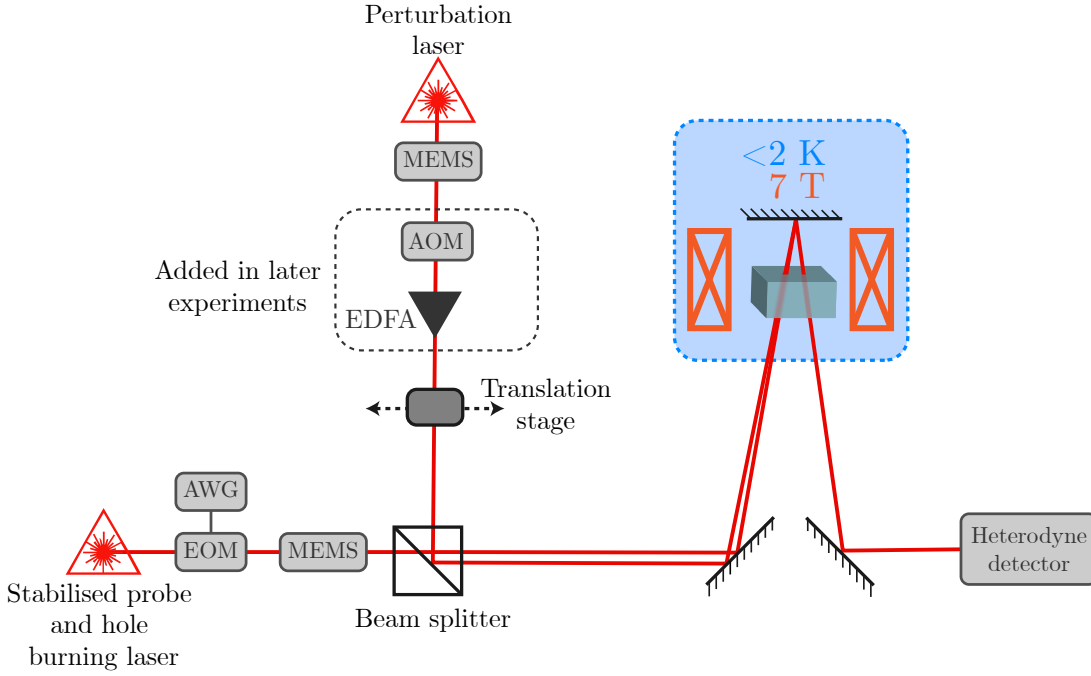


Figure 3.3: The general setup used in all experiments. I added the dashed box containing the EDFA and AOM to later experiments for finer control of power and turn on time.

to produce phonons. The probing path used a narrow linewidth laser and an electro-optic modulator (EOM), with the signal turned off using a Micro-ElectroMechanical Systems (MEMS) switch. The EOM allows for modulation of the signal's frequency, while the MEMS switch gates the laser on and off on the time scale of $100\ \mu\text{s}$ with very good extinction. The second path was for making perturbations by applying short pulses at a tuneable range of frequencies around the 1538 nm optical transition. I could turn this laser on and off using a MEMS switch, however, for some later experiments an acousto-optic modulator (AOM) was included. The AOM has much faster turn on/off times than the MEMS switch at $\sim 100\ \text{ns}$, however, only blocks 99% of the signal, so needs to be used in conjunction with the MEMS to block the light fully. This setup also included an Erbium Doped Fibre Amplifier (EDFA), which can be used to increase the power of the signal.

For certain experiments, I needed to vary the distance between the two beams. To do this, the focusing lens in the perturbation path was placed on a translation stage to linearly translate the beam on the beam splitter that combined the two paths, and therefore on the crystal. I positioned the probing beam at the centre of the sample, and I would translate the perturbing beam along the 10mm side of the sample.

A typical experiment involved inputting light on the order of 1 mW in power, and after travelling through the cryostat, the light was coupled into a detector. As the probe pulses were low intensity and short (less than μs), the signal was measured using a modified heterodyne detection technique as in [39]. In this method a modulated beam is mixed with the output, and the beating of the signal is measured. A high frequency detector is used to take measurements of the spectrum. The spectrum measured by this detector is dependent on both the absorption of the atoms (the imaginary part of the refractive index) and the dispersion (the real part of the refractive index). The combination of absorptive

and dispersive effects results in a ‘dip’ in the signal from the most highly absorbing part of the inhomogeneous line (shown in Figure 3.4). Careful post processing can extract only the absorption line-shape, but for my measurements, the raw data gave sufficient information and I did not post-process it.

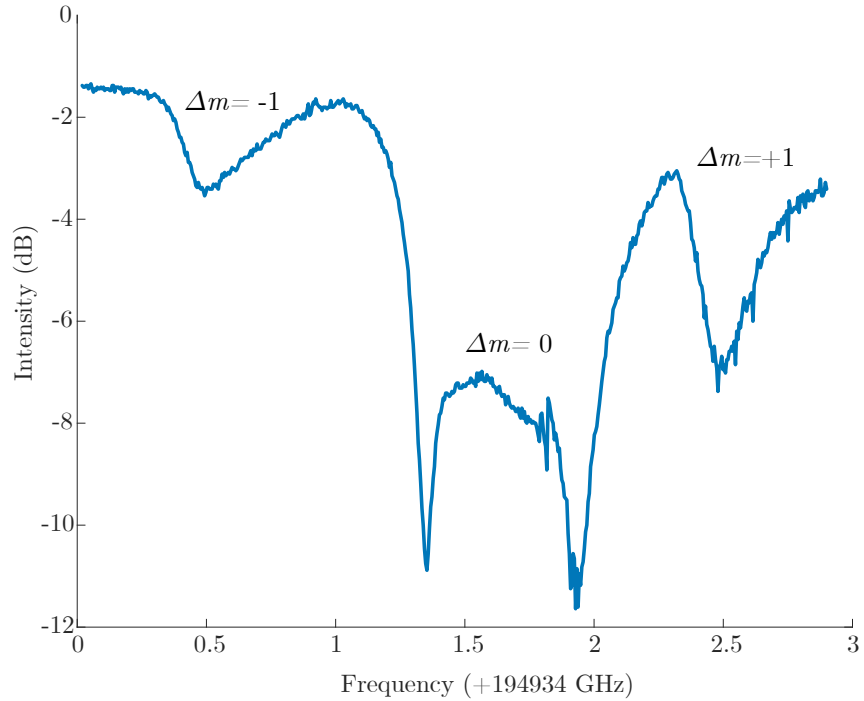


Figure 3.4: The measured transition spectrum using a high frequency detector. The high intensity $\Delta m = 0$ band has a dip in the middle. The true absorption of the centre of line is approximately -20 dB.

3.2 Experimental techniques

Now that I have explained the experimental setup, I am going to describe the experimental techniques I have used in this thesis.

3.2.1 Spin polarisation

The previous measurements of phonon effects that motivated this project occurred during a particular type of spectral preparation called spin-polarisation. Under normal experimental conditions, the ions will be populating the hyperfine states equally (thermal equilibrium). Spin polarisation is a process that moves these ions to a single hyperfine state. This is achieved by sweeping a high-intensity laser over the atoms to excite the $\Delta m = +1$ transition as shown in Figure 3.5. Each of these transitions excites the atom (initially with spin projection m) to the higher energy corresponding to spin projection $m + 1$. When the atom falls to the ground level, it is more likely to fall to an energy level with the same spin projection as the excited state, which is one level higher than the atom was originally in. Repeating this process pushes all the atoms to the highest energy level of the ground state, removing the $\Delta m = 1$ transitions.

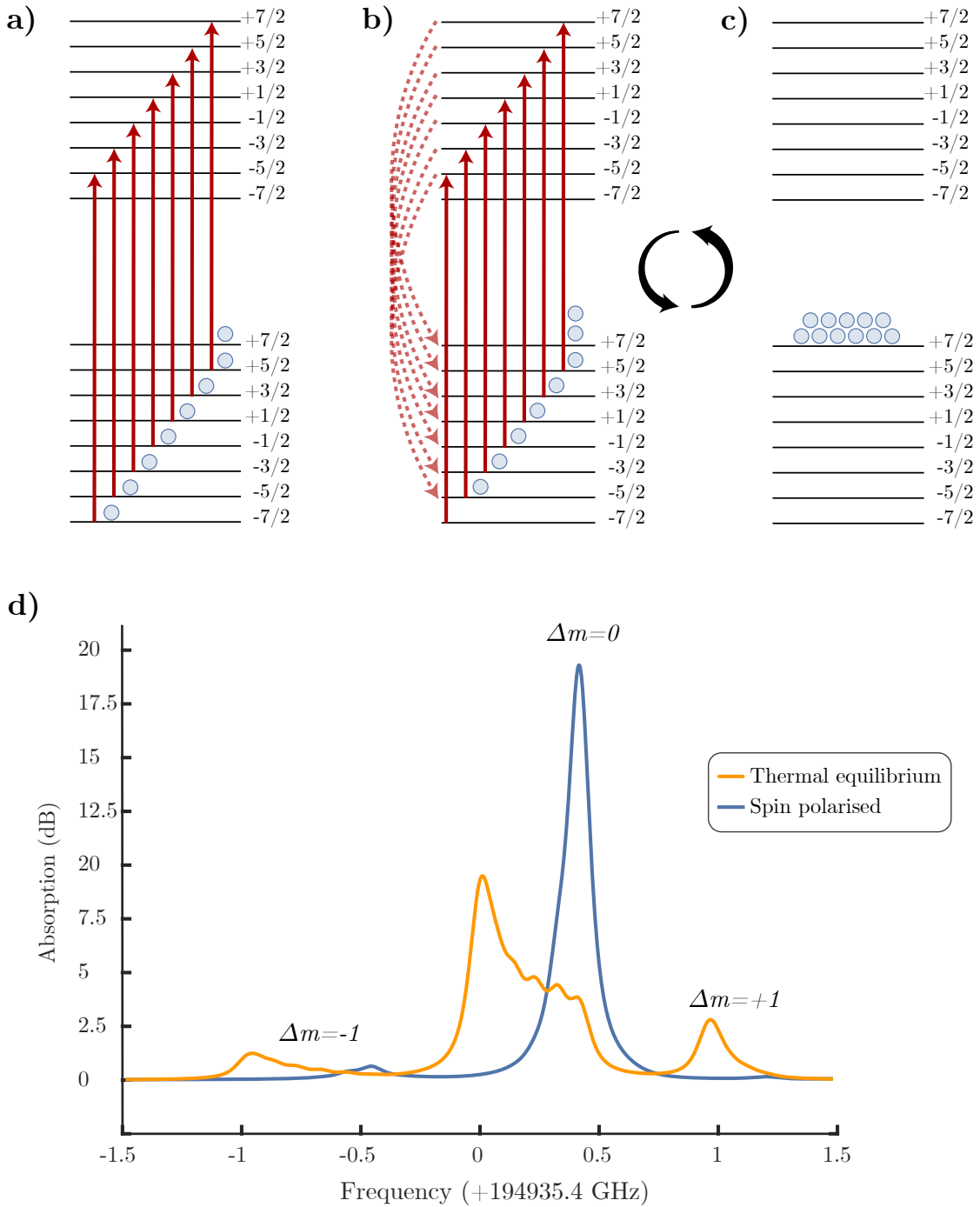


Figure 3.5: The spin polarisation process in erbium. The laser sweeps across the $\Delta m = +1$ transition, as shown in a), exciting the atoms to a level spin greater by 1. The atoms then fall back, most commonly on a $\Delta m = 0$ transition, as shown in b). By repeatedly sweeping, the atoms step up the energy levels, with almost all atoms eventually in the highest energy level as shown in c). A simulation of the spectra (courtesy of James Stuart) resulting from spin polarisation is shown in d). The $\Delta m = +1$ transition has disappeared, and the $m_I = +7/2$ hyperfine level of the $\Delta m = 0$ transition is highly populated.

Spin polarisation places all the atoms at the same hyperfine level. This is a useful preparation technique in erbium crystals for several reasons. First, it narrows the line and results in higher absorption, which is useful for quantum memory protocols. Second, it increases the hyperfine lifetime because, with all the atoms in the same level, spin flip flops are suppressed. This can be used to increase hole lifetimes from one minute to three in $\text{Er}^{3+}:\text{Y}_2\text{SiO}_5$. For this thesis, I made several measurements with the erbium ions spin polarised, but the majority of measurements used the ions in thermal equilibrium.

3.2.2 Hole burning

Hole burning measurements were the main technique I used to measure the effect of phonons. This involved observing how a hole burnt in one of the frequency bands would react to the perturbing laser. To do this, I burnt a hole in the $\Delta m = -1$ band at the centre of the crystal using the probing beam path. The laser was held at a fixed frequency for approximately 100 ms to pump the ions at that frequency into non-resonant states. The hole was then probed by sending a short pulse on resonance with the hole. Taking the Fourier transform of the pulse reveals the spectra of the hole. The intensity of this pulse was low to minimise filling in the hole with the probe. With this intensity, it was possible to repeatedly sweep out the hole 100 times without decreasing its size. I varied the frequency, burn start time and length depending on the experiment.

To measure the effect of perturbing the atoms on a spectral hole, the general method follows that is shown in Figure 3.6. First, I probed the atoms 100 times before the hole was burnt to establish the background. Then, I burnt the hole and immediately probed it 100 times. Next, I perturbed the system (by exciting atoms using the perturbation laser) and re-probed the atoms.

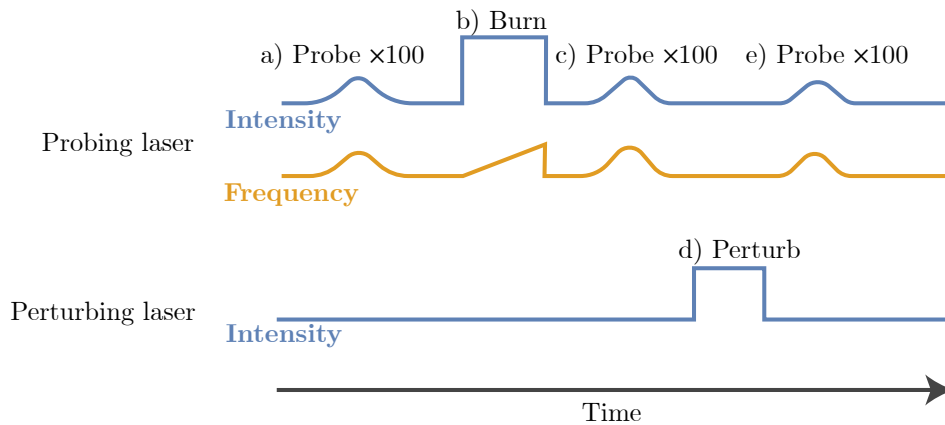


Figure 3.6: The sequence used when taking hole fill-in measurements. The reference probe is taken (a), then the spectral hole is burnt (b), and the hole probe is taken (c). The perturbation pulse is then applied (d), and the hole after perturbation is probed (e). Each probe takes 100 measurements of the spectrum.

An example of a hole burning measurement is shown in Figure 3.7. This measurement was taken with the beams overlapped, and the perturbation laser applied for 100 ms, with the mean of the 100 probes plotted. The reference spectrum is the Fourier transform of the input pulse shape. When the hole is burnt into spectra, there is a peak in the intensity from the decrease in absorption. After the perturbation is applied, the intensity of the

hole is decreased as the perturbation will restore the atoms toward equilibrium, filling in the hole. The hole burning measurement is therefore a measurement of the number of atoms that change in energy because of the perturbation.

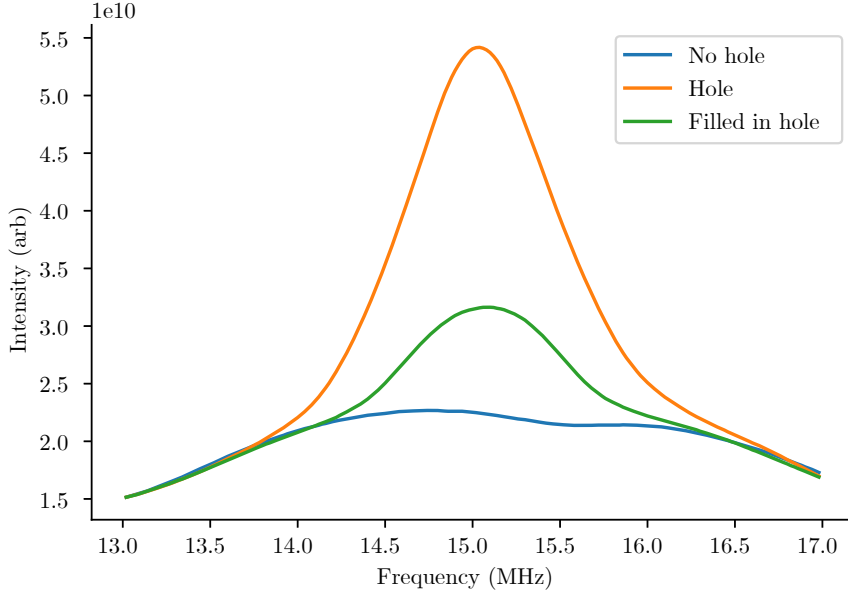


Figure 3.7: The measured light intensity at different points in the hole burning process. Plots made are the mean of 100 measurements, with a 100 ms burn time.

An issue with this method is that hole intensity does not linearly correspond with the number of atoms in the hole. The intensities from the hole measurements can be related to the number of atoms using the Beer-Lambert law. The Beer-Lambert law gives the intensity of light transmitted through a material as

$$I(f) = I_0 e^{-\mu g(f)l} \quad (3.1)$$

where I_0 is the initial light intensity, l is the length of the crystal, f is the frequency, μ is a constant attenuation coefficient and $g(f)$ is a line-shape function. Assuming all absorption has the same cross-section (σ), then the attenuation coefficient can be written as $\mu g(f) = \sigma n(f)/V$ where $n(f)$ is the number atoms in the volume V . The ratio of two intensity measurements is therefore

$$\frac{I_1(f)}{I_2(f)} = e^{\frac{l\sigma}{V}(n_2(f)-n_1(f))} \quad (3.2)$$

$$(3.3)$$

which can be rearranged to give the number difference between two intensity measurements

as

$$n_2(f) - n_1(f) = \text{Log} \left(\frac{I_1(f)}{I_2(f)} \right) \frac{V}{l\sigma} \quad (3.4)$$

The total number difference is given by integrating this over frequency. Using n_0 to be the number of atoms before burning a hole, n_h to be the number of atoms left after burning the hole, and n_f to be the number of atoms after the perturbation, the percentage change of atoms over the hole is therefore

$$\Delta\% = 100 \times \frac{n_f - n_h}{n_0 - n_h} = 100 \times \frac{\int \text{Log} \left(\frac{I_h(f)}{I_f(f)} \right) df}{\int \text{Log} \left(\frac{I_h(f)}{I_0(f)} \right) df} \quad (3.5)$$

where I have assumed that the initial hole burn has removed nearly all the atoms. I used this formula for all hole fill-in measurements. The power of the laser can vary between each of the probing sequences, so the three intensity measurements were normalised so that the intensities before the hole matched.

This percentage calculation requires that the perturbed hole intensity is not below the reference intensity and does not exceed the unperturbed hole intensity. To ensure this would not happen, the perturbed hole intensity measurements were capped between the intensity of the other intensity measurements.

Standard error propagation is not appropriate due to the integration and log ratios of intensity in the formula. Instead, errors of the hole measurements were estimated using Monte-Carlo simulations. These were made using the following steps. I first took the error of the intensity measurements over frequency for each probe. Based on these errors, a random offset following a normal distribution was generated, and added to the mean value of the intensity. The percentage fill was then calculated using the generated intensities. Repeating this 1000 times creates a distribution of hole fill values. The standard deviation of this distribution was used as the error. This process was applied to each hole measurement.

The hole burning measurements may have some additional hole fill-in due to the probing sequence as the size of the hole is determined by measuring the transmission of light through the sample, and there is a possibility that these measurements could themselves cause hole-burning, which reduces the size of the signal. To test for this, I repeated the hole burning measurement, but with 500 probes. I have compared the mean of the first 100 measurements with the last 100 measurements in Figure 3.8, and found that the measurement process had little effect on the intensity of the hole, with the measured hole fill-in percentage varying by 0.7%.

3.3 Chapter summary

In this chapter I have discussed the experimental setup and techniques used in this thesis. I started by discussing crystal mount. The key information from this going forward is that rotations are being made by rotating about the D2 axis, with a 7 T field applied

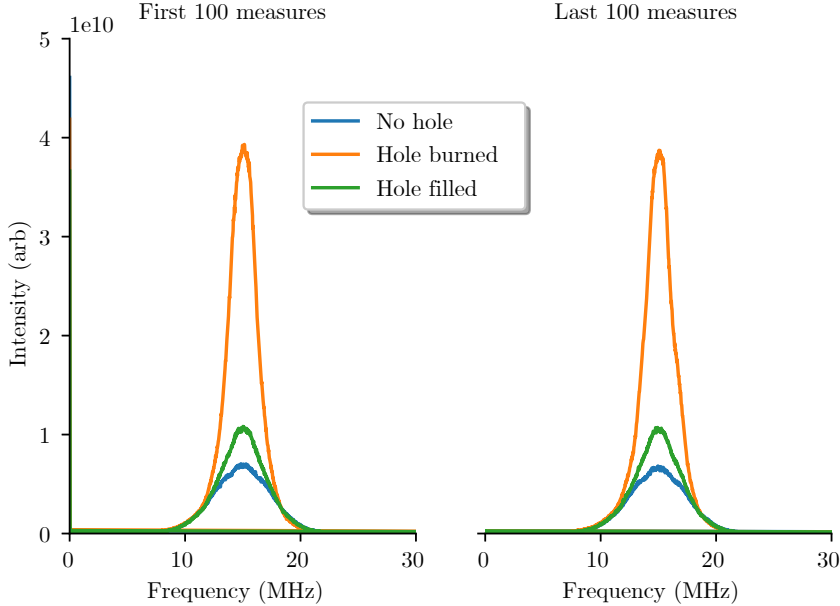


Figure 3.8: The mean measurements taken over a period of 500 probes. The left shows the mean of the first 100 measurements, while the right shows the mean of the final 100 measurements. The two means give hole fill-in values that vary by less than 1%, indicating that the probe power does not significantly fill the hole over the 100 probes used for measurements.

along the D1 axis. I then described the laser input setup, and the tools used within this setup, showing that the detection method inverts the $\Delta m = 0$ peak in the transition spectrum. Finally, I described spin polarisation, and the hole burning technique used to make measurements throughout this thesis. I confirmed that measurements used do not significantly affect the hole burned. In the next chapter, I will determine the type of interaction that caused decoherence.

Confirming phonon induced population redistribution in Er³⁺:Y₂SiO₅

In this chapter I will determine if phonons are being induced by optical excitation in Er³⁺:Y₂SiO₅. I will start by describing and recreating the initial experiment indicating that these interactions were occurring. I will then run experiments to distinguish if the phonons are being induced by increasing the distance of the interactions.

I was assisted in running the experiments in this chapter by James Stuart. James taught me how to set up and run the experiment. He provided me with prototype code that I modified to run the experimental sequences. All measurements and analysis in this chapter are entirely my own work.

4.1 Recreating the observed effect

My project was motivated by observations made by James Stuart in 2019, while performing the initial spectral preparation steps required for his experiments on an erbium based quantum memory. While optically pumping the sample to spin polarise the atoms, James saw that when the intensity of the pumping laser was increased, the spin polarisation was reduced. This was unexpected, as the higher intensity should either have no effect, or more rapidly spin polarise the sample. This suggested that the process of spin pumping was redistributing population amongst the hyperfine levels through an unwanted interaction. It was proposed that, as the interaction was induced by optical excitations, phonons could be the source.

I first wanted to recreate this observation by confirming that a perturbation would cause a loss of spin polarisation. To do this, I followed the sequence shown in 4.1 a). As described in the previous chapter, the sample was spin polarised by sweeping a laser over the $\Delta m = +1$ band, which pumps the ions into the $+7/2$ state. I then burnt a hole in the $\Delta m = 0$ band for 100ms to see how this excitation changed the polarisation, taking spectra after the burn. I then repeated the 100 ms burn and spectra measurements.

The measurements of the spin polarisation experiment are shown in Figure 4.1(b)). As the number of perturbation pulses increased, the peak in intensity of the $\Delta m = 0$ band shifted slightly to a lower frequency, as did the lower intensity $\Delta m = -1$ peak. This is

because the perturbation redistributed the ions from the $+7/2$ hyperfine level (which has the highest transition frequency), spreading them over the other hyperfine levels. This means the lower energy hyperfine levels were becoming populated. This matches James' observation of the spin polarisation becoming worse with increased excitation. Given the lifetime of the spin polarisation is much longer than 1 minute, this measurement confirms that the excitation of ions by the perturbation pulse is redistributing population closer to thermal equilibrium.

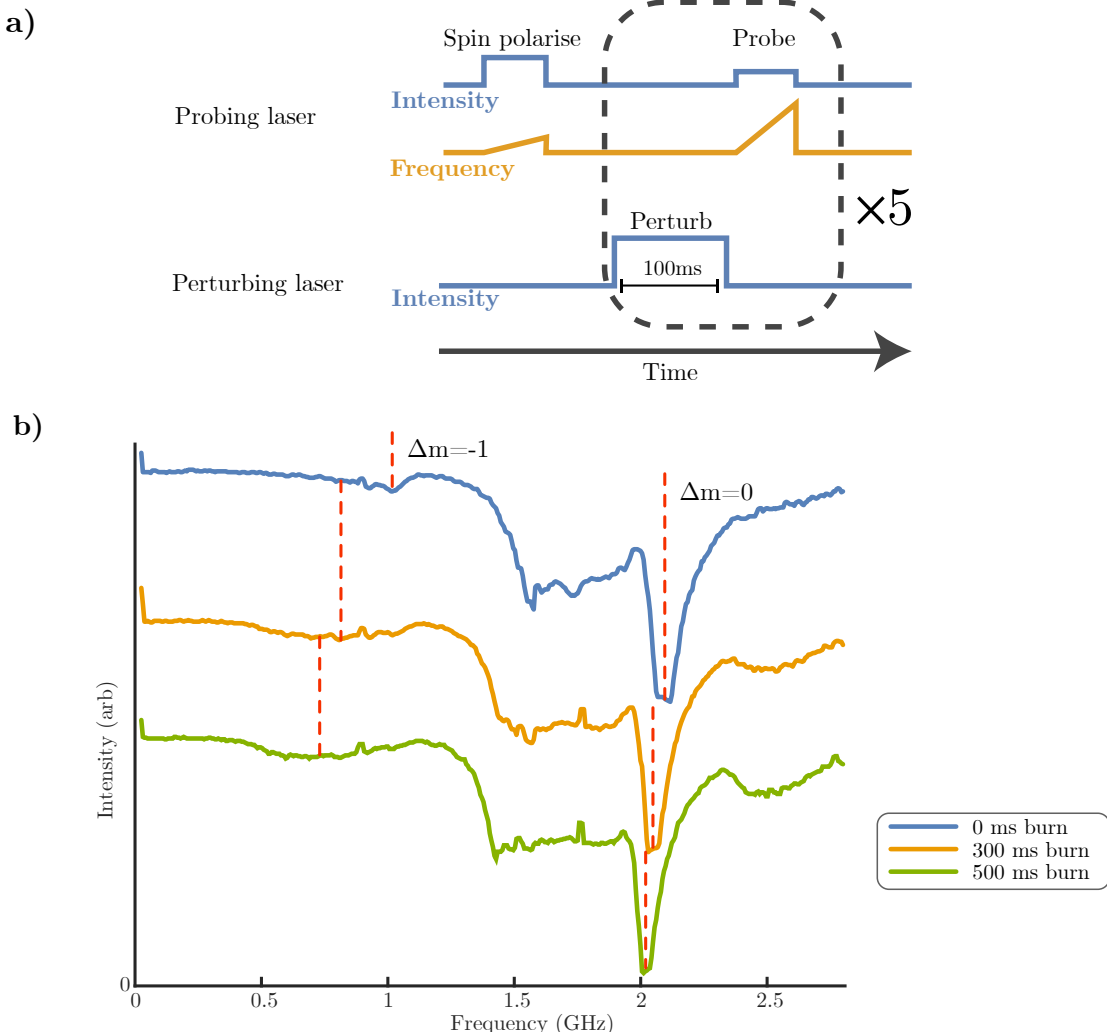


Figure 4.1: The pulse sequence used to drive the two lasers used for the perturbed spin polarisation experiment is shown in a). The 0 ms burn, 300 ms burn, and 500 ms burn are shown in b). As described earlier, the asymmetric shape of the $\Delta m=0$ spectrum is due to the combination of absorption and dispersion. The spectrums can be seen to shift to left, as the atoms repopulate the hyperfine levels.

The source of the loss of spin polarisation could be from a combination of the following three interactions. The first possibility is fast spin-spin interactions acting during the hole-burning pulse, which effectively optically pump atoms that are not resonant with the laser. The second is interactions with equilibrium phonons, produced because the optical excitation heats the crystal. The third possibility is non-equilibrium phonons, which would be emitted by excited atoms. Both phonon processes would result in the

spin-polarised atoms absorbing a phonon and falling to another hyperfine level. Of these, the spin-spin process can be discarded because the spin lifetime (minutes) is much longer than the hole-burning time (100 ms), indicating that the process is most likely phonons. Phonons can be confirmed using the different length scales of the processes. Phonons are a travelling excitation, and act over ranges dependent on the lifetime of the phonons - in some materials this can be metres. Spin-spin interaction fall off significantly over distance and are negligible on scales more than microns. As such, a method for only measuring the effect of phonons is to excite atoms far from the probed atoms.

4.2 Confirmation of phonons by translating the beam

With confirmation that the perturbation pulse would cause a redistribution of the hyperfine population, I wanted to confirm whether phonons induced these transitions. To do this, I ran an experiment increasing the distance between the perturbed and probed atoms. To measure the magnitude of the interaction, I used the hole fill-in method discussed in Chapter 3. The perturbed hole measurement is equivalent to measuring the spin polarisation from the previous section. This is because both spectral preparations change due to a redistribution of the hyperfine population. However, the hole-burning method was more suitable for studying the effect because the percentage change of atoms can be calculated using Equation 3.5. I took the experimental data by spatially overlapping the beams and then running the hole-burn perturbation sequence, with perturbation times of 100 ms. I repeated this, with the perturbation beam translated after each measurement. The measured hole fill percentage with beam distance is shown in Figure 4.2. The hole was most filled when the two beams were overlapped, with the effect of the perturbation then decreases as the distance between the beams is increased, appearing to flatten at approximately 20% hole fill-in. The fill ratio drops to 0% as the beam is moved off the edge of the crystal (the orange line).

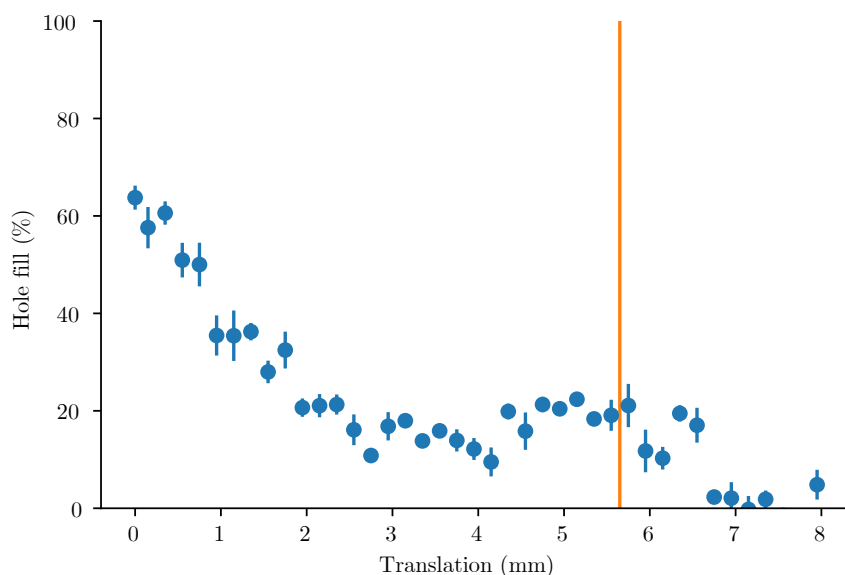


Figure 4.2: Hole fill-in data with beam difference. The orange line is the edge of the crystal. Although reduced, the perturbation still fills the hole in from millimetres away.

When the beams are overlapped, the perturbation pulse can pump atoms into the spectral hole or fill it in via short-range excitation induced interactions. As both the probe and perturbation beams have a non-zero diameter, the perturbation beam has some intensity that overlaps with the centre of the probe beam even when they are separated. This means the perturbation can cause some direct filling of the hole burnt by the probe. To eliminate this as a reason for the hole filling, and to confirm that the hole filling is caused by phonons travelling from part of the crystal to another, I need to eliminate the possibility of residual beam overlap optically pumping the ions back.

4.2.1 Hole fill-in induced by the edges of the beam

To estimate the fill-in from the edges of the beam, I need to know the power profile of the beam, and the relation between hole fill-in and power.

To determine the beam width, I used the knife-edge method. This involved placing a blade on a translation stage at the focal point of the beam and moving the blade through the width of the beam, taking measurements of the transmitted power at each position. Laser beams are normally considered to be Gaussian, however, my beam was clearly non-Gaussian. The best fit to the data was obtained by modelling it with a cumulative Lorentzian distribution. This gave the following model:

$$P = P_{max} \left(\frac{1}{2} - \frac{1}{\pi} \arctan \left(\frac{x - x_0}{\gamma} \right) \right) \quad (4.1)$$

where P_{max} is the maximum power, x is the knife edge position, x_0 the centre of the beam, and γ is the half width at half maximum. The measured data and best fit are plotted in Figure 4.3.

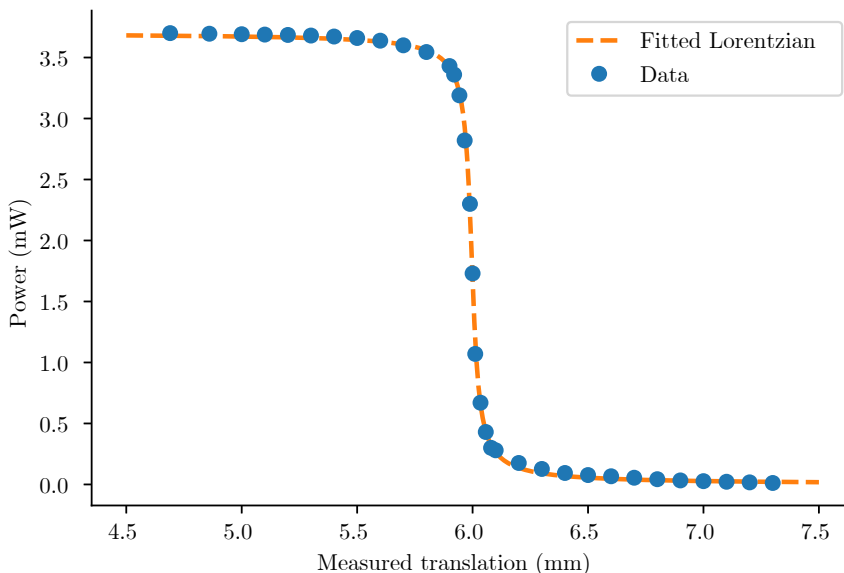


Figure 4.3: Knife edge measurement of the diameter of the perturbation beam. The fitted model has best fit with $\gamma = 0.024$ mm.

I ran the hole burning sequence at several different perturbation beam powers to determine

the relation between power and hole fill-in. The measurements are shown in Figure 4.4. The perturbation pulse is comparable to a shortening of the hyperfine lifetime, thus filling in the hole. Assuming that the lifetime shortening is linear with intensity, I can model the relation between hole fill and power as an exponential. This assumption is somewhat simplistic, as the hole-burning dynamics at the perturbation frequency will also change with intensity, but it is sufficient for this experiment. I use the following model:

$$\Delta\% = p_{max}(1 - e^{-aP}) \quad (4.2)$$

where p_{max} is the maximum hole fill-in, P is the power, and a is a fitting parameter. The best fit is shown in Figure 4.4. Using this model and information about the beam width, I can estimate the beam intensity at different radii and determine expect hole fill-in from the beam edges. As perturbing at high powers can cause holes to be burnt, and therefore fewer atoms to be hit, I have assumed that the maximum hole fill is less than 100%.

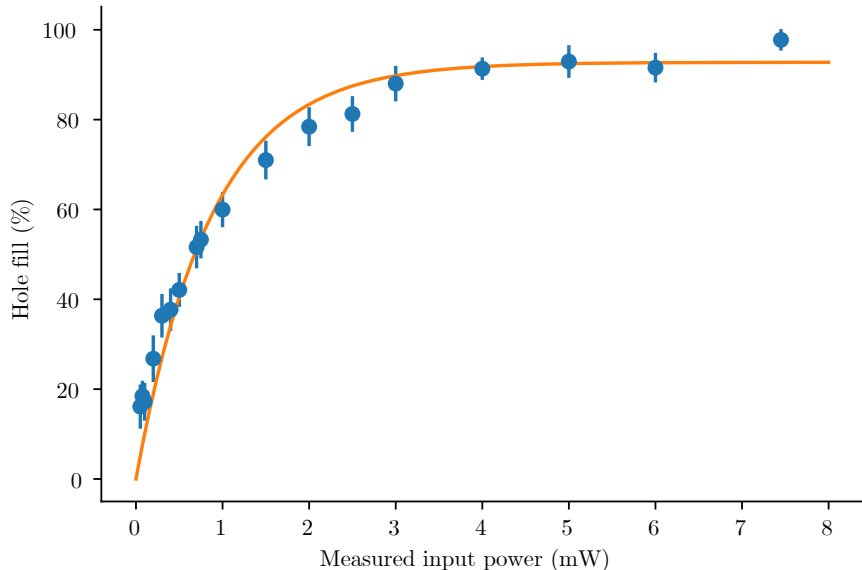


Figure 4.4: Plot of hole fill-in data with varying intensity. Data is shown in blue, while the model is in orange. The best fit has $p_{max} = 93 \pm 2\%$, and $a = 1.07 \pm 0.1 \text{ mW}^{-1}$.

With a relation between beam power and hole fill-in percentage, I can model how much the hole will fill in at different translations. Using a Lorentzian profile, the beam power as a function of radius is

$$P(r, \gamma) = P_0 \left[1 + \left(\frac{r}{\gamma} \right)^2 \right]^{-1} \quad (4.3)$$

where r is the radial distance, and P_0 is the central power.

Modelling the power with Eq 4.3 and the hole fill-in at that power by Eq 4.2 gives the calculated line in Figure 4.5. The beam width is much smaller than observed range of

phonon excitation, and the modelled effect due to beam overlap drops off rapidly. This data clearly indicates that the hole-fill-in effect seen must be due to phonons.

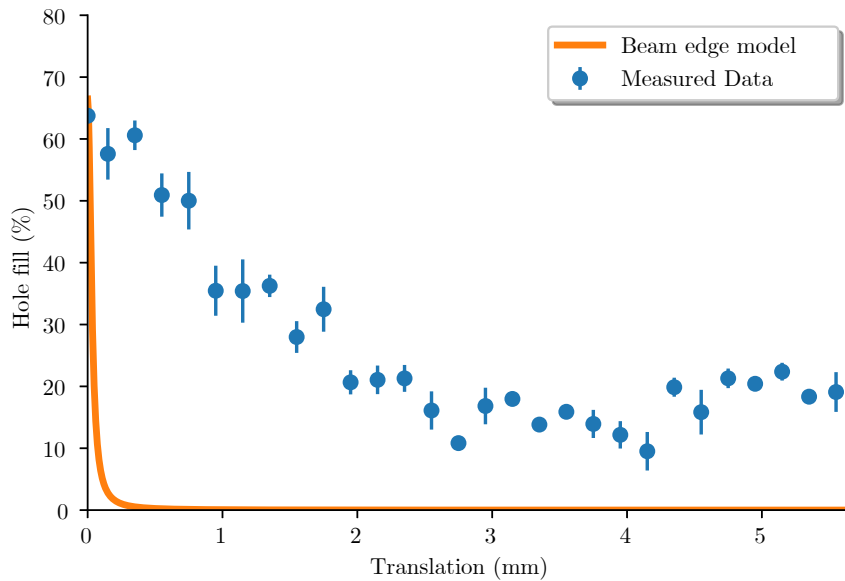


Figure 4.5: Model of hole fill-in caused by the overlap of the perturbation beam edge with the probe (orange line) compared to the measured hole fill-in. As the model drops off much faster than the measured values, phonons must be the source of the hole fill-in.

4.3 Chapter summary

In this chapter, I have shown that phonons will redistribute population in $\text{Er}^{3+}:\text{Y}_2\text{SiO}_5$. I did this by increasing the distance between perturbed atoms and probed atoms, observing interactions that were maintained over lengths of millimetres. I then created a model of the interaction dependent only on the non-zero width of the perturbation beam. This model dropped off over distance much faster than the observed data, removing the possibility that the observed hole fill was due to beam overlap. Phonons are the only interaction in this material that act over these long distances, confirming their existence. In the next chapter, I will run experiments to determine the properties of the phonons, and whether they are equilibrium or non-equilibrium.

Characterisation of phonons

In this chapter I will further investigate the properties of the phonons induced in $\text{Er}^{3+}:\text{Y}_2\text{SiO}_5$. I will start by determining if the phonons are equilibrium or non-equilibrium. I then discuss the linewidth of the phonons, and the possible transitions that contribute to the linewidth. I then describe measurements I made to analyse the propagation properties of the phonons. I will finish the chapter by showing measurements of coherence times using photon echoes, and a photon echo measurement to determine the lifetime of created phonons.

I was assisted in running the experiments in this chapter by James Stuart. James taught me how to set up and run the experiment. He provided me with prototype code that I modified to run the experimental sequences. All measurements and analysis in this chapter are entirely my own work.

5.1 Frequency dependence of the phonon relaxation

In the previous chapter, I confirmed that the anomalous hole filling is due to phonons produced by optical excitation. However, it was not clear whether these phonons are equilibrium phonons from the laser heating the crystal, or the perturbation generating non-equilibrium phonons resonant with the atoms in the hole. The difference between equilibrium and non-equilibrium phonons is their frequency. Equilibrium phonons will conform to the wide-bandwidth thermal distribution, while non-equilibrium phonons will match the frequency of the transition that created them. To determine the type of phonons induced, I needed to vary the frequency difference of the probe and perturbation.

I created a frequency difference between the probe and perturbation by probing in the $\Delta m = -1$ band, and perturbing atoms elsewhere in the line. I took measurements of the hole fill-in with the perturbation pulse at different frequencies across the optical spectrum, with the beams separated by 1 mm to ensure that only phonons were having an effect. When atoms are perturbed from the $+7/2$ hyperfine state, most possible phonons produced would not be resonant with the $-7/2$ hyperfine state, unless the phonons have a linewidth on the order of GHz.

A plot of the measured hole fill-ins at different frequencies is shown in Figure 5.1, with the transition spectrum overlaid. As I moved the perturbation pulse across the line, the level of hole filling was more dependent on the number of atoms I was hitting, rather than the frequency of the transition. This is clear as the $\Delta m = \pm 1$ transitions equally filled in the hole, despite the $\Delta m = +1$ being GHz away in frequency. These findings

mean that either non-equilibrium phonons are being formed with a linewidth of at least GHz, or the perturbation is raising the temperature of the crystal and creating equilibrium phonons.

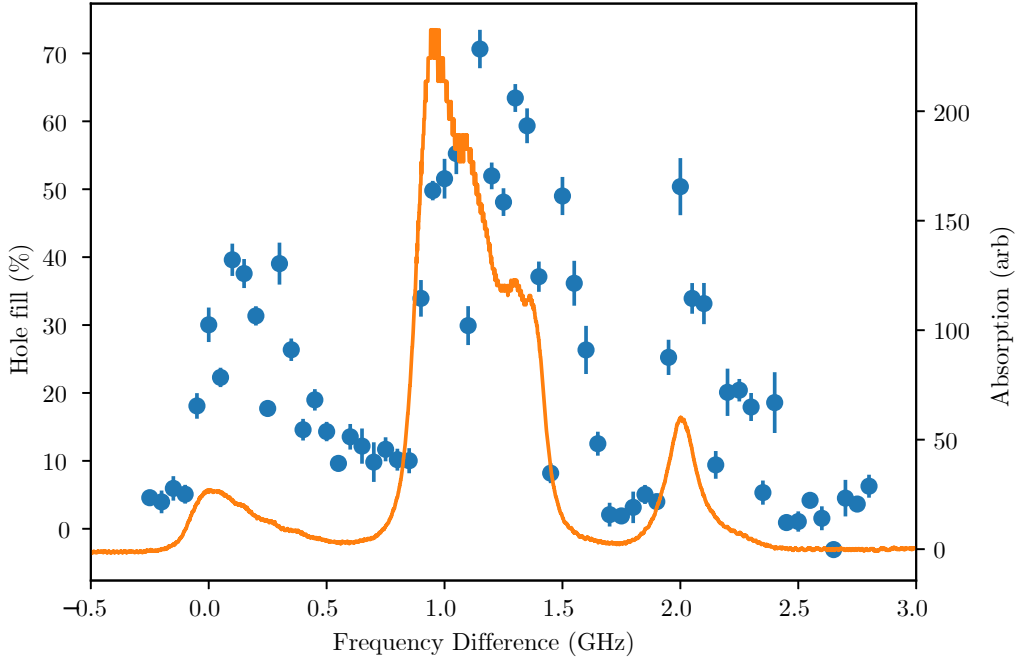


Figure 5.1: Measured hole fill perturbing at different frequencies while the orientations are overlapped. The orange line is an overlay of the transition spectrum that has been offset by 194.94 THz, to show the frequency of the perturbed atoms. The x-axis is the frequency difference between the perturbed and probed atoms, with the hole burnt at 0 GHz.

5.2 Discerning the phonon type

I will be considering the possibility that the phonon distribution is wide by producing phonons much further detuned than was possible by just burning across the line. If the perturbation pulse is inducing non-equilibrium phonons, then these phonons will match the frequencies of the perturbed atoms. If the perturbed atoms are at a different frequency than the burned hole, the phonons will not be resonant with transitions to the ground state, and the hole will be unchanged. If equilibrium phonons are being induced, then the hole will fill in no matter the perturbation frequency, as the increased temperature creates phonons over a large range of frequencies (as shown in Figure 2.11). In $\text{Er}^{3+}:\text{Y}_2\text{SiO}_5$, it is possible to produce phonons at a controllable frequency offset from the probed atoms, because the erbium site has two possible orientations. When the crystal is tilted, the magnetic field is no longer along the D1 axis, and the ions in these two sub-sites have different energy level structures. I can then probe the lower frequency sub-site while perturbing the higher frequency sub-site. The maximum frequency difference of the lowest frequency transition that could be producing phonons (from the $^4\text{I}_{15/2}(Z_1, \uparrow)$ level) is 16 GHz as described in Chapter 3 and shown in Figure 3.1.

The probe and perturbation beams were separated by 1 mm to ensure that phonons were the only interaction filling the hole. The hole was burnt into the $\Delta m = -1$ band of

the lower frequency orientation, and the perturbation frequency was set to the centre of the $\Delta m = 0$ band of the upper frequency orientation. I then ran the hole burning and perturbation sequence, starting with the rotation such that the two orientations were overlapped in frequency. I would then rotate the sample and take spectra to determine the frequency separation of the two orientations, adjusting the burn and perturbation frequencies to be hitting the same atoms in the line.

The experimental results are shown in Figure 5.2. As the frequency difference between the two orientations was increased, the measured hole fill decreased. This confirms that the perturbation is inducing non-equilibrium phonons, with the higher frequency phonons being unable to resonantly excite the atoms in the hole back into equilibrium.

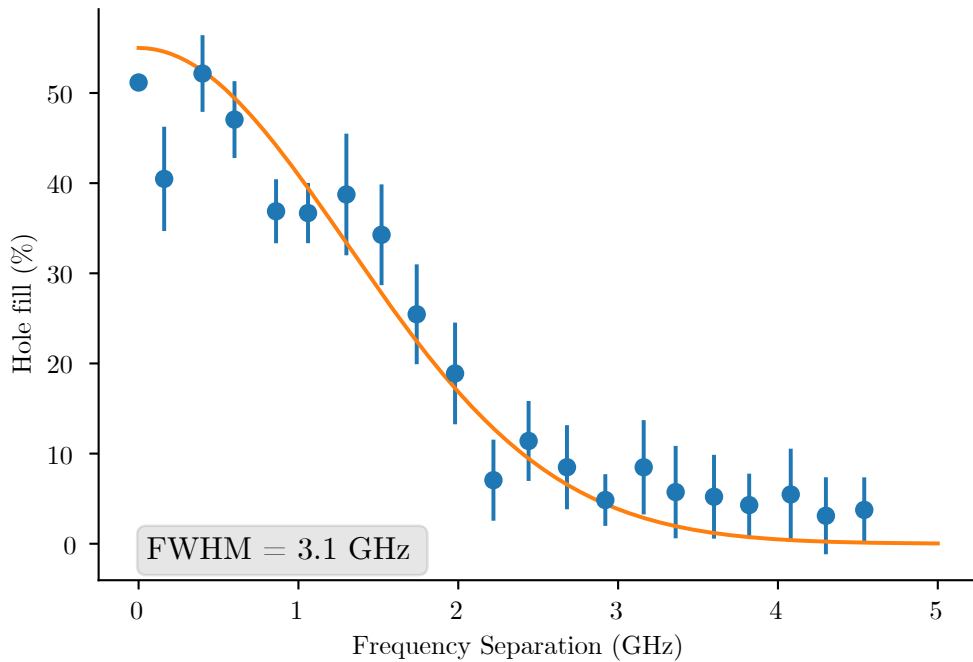


Figure 5.2: Measured hole fill-in at different crystal rotations. The x-axis is the frequency separations between the two orientations of erbium in the crystal. The orange line is a best fit Gaussian centred at 0.

I fit a Gaussian to the data, as shown in Figure 5.2. The phonon distribution is not necessarily Gaussian, however it is useful to give an idea of the frequency range of the induced phonons. The fitted Gaussian has a full-width half maximum of 3.1 GHz in the optical frequency. This corresponds to a range of 2.7 GHz in the transition I believe to be producing phonons (${}^4\text{I}_{15/2}(Z_1, \uparrow)$ to ${}^4\text{I}_{15/2}(Z_1, \downarrow)$). There are two possible types of broadening that could contribute to this linewidth - the lifetime limited homogeneous linewidth, and the inhomogeneous linewidth. Estimates of the lifetime limited linewidth of individual phonons in $\text{Er}^{3+}:\text{Y}_2\text{SiO}_5$ and other rare-earth doped crystals range from 10 kHz-MHz, while the inhomogeneous linewidth depends on the inhomogeneous width of the atoms that produced the phonons.

In Chapter 2, I explained that the phonons are most likely from the ${}^4\text{I}_{15/2}(Z_1, \uparrow)$ to ${}^4\text{I}_{15/2}(Z_1, \downarrow)$ transition. We can calculate the phonon frequency range using a model of

these energy levels in $\text{Er}^{3+}:\text{Y}_2\text{SiO}_5$ [22], since the relevant levels have not been measured experimentally.

I simulated the levels shown in Figure 5.3 with an applied field of 7 T. There are many pathways for atoms to fall into these levels, so all the levels should be evenly populated, regardless of the optical state the atoms start in. Considering just the strongest $\Delta m = 0$ transitions, which maintain spin projection, the range of the transition frequencies is 2.99 GHz, covering much of the phonon linewidth observed in experiments. The crystal field models are only approximate, so measurements of the hyperfine levels would be needed to confirm this range. The observed phonon linewidth can be simulated, assuming each of the transitions is equally strong and follows a Gaussian distribution. The linewidths of these individual transitions would overlap if there is enough inhomogeneous broadening in the atoms.

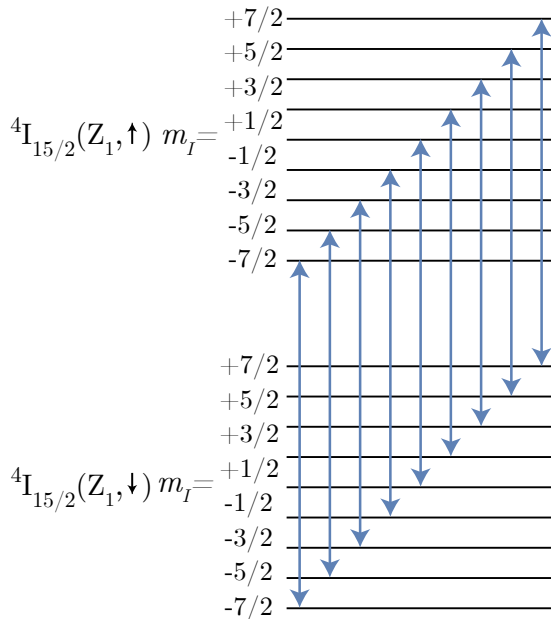


Figure 5.3: The two lowest energy levels of the crystal field, and the hyperfine splitting. The transitions with $\Delta m = 0$ are drawn, as these are the most likely phonon paths under experimental conditions.

The primary source of inhomogeneous broadening is because of variations in the crystal lattice. In this crystal, the optical inhomogeneous linewidth is 150 MHz. It is reasonable to assume that the electron spin transition will not be wider than this, although it could be narrower. Another source of inhomogeneous broadening is variations in the experiment. The magnetic field in the cryostat varies by approximately 5×10^{-4} T over the length of the sample. Running crystal field simulations with this magnetic field variation finds that the separation between the ${}^4\text{I}_{15/2}(Z_1, \downarrow)$ and ${}^4\text{I}_{15/2}(Z_1, \uparrow)$ levels would vary by 50 MHz over the crystal. Adding the additional inhomogeneous broadening, the spectrum of phonons is shown in Figure 5.4. If this was the true phonon spectrum, I would expect to see fluctuations in the hole fill-in in Figure 5.2 for small (hundreds of MHz) changes in frequency, due to the different peaks in this spectrum. It is possible these are not seen as the lines could be more inhomogeneously broadened than I have accounted for. Additionally,

the inclusion of phonons from $\Delta m = \pm 1$ transitions, and higher energy transitions would occupy some of the gaps in frequency. I have also not considered transition strength. Overall, the main conclusion that can be drawn from this model is that phonons produced from the ${}^4\text{I}_{15/2}(Z_1, \uparrow)$ state relaxing are spread over frequencies matching the measured phonons.

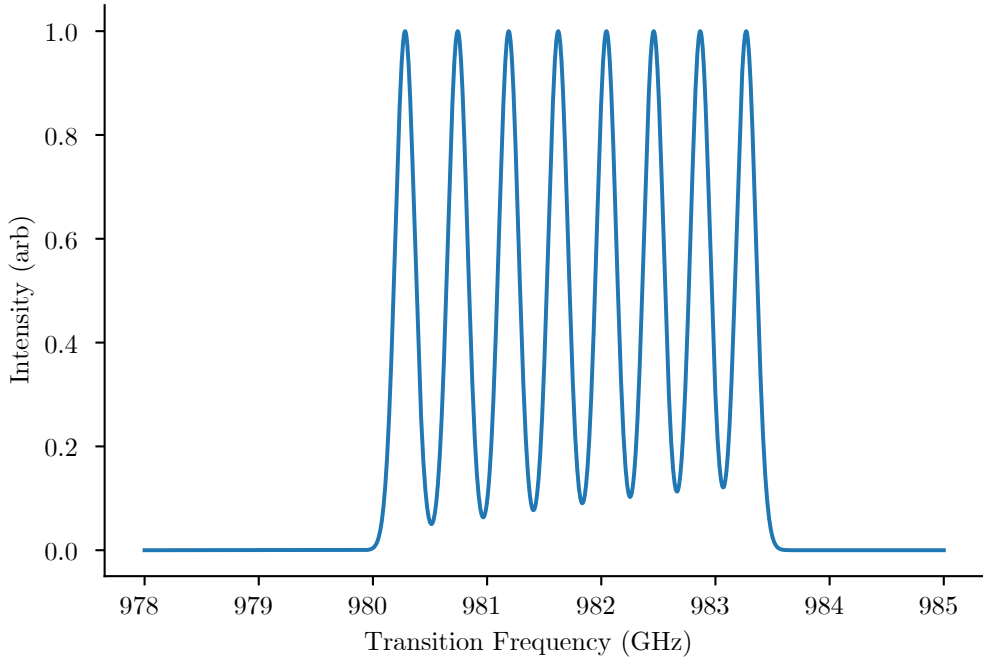


Figure 5.4: The sum of the phonon frequencies from transitions between the ${}^4\text{I}_{15/2}(Z_1, \uparrow)$ and ${}^4\text{I}_{15/2}(Z_1, \downarrow)$ levels including 200 MHz of inhomogeneous broadening.

5.3 Propagation properties

The propagation properties of non-equilibrium phonons in $\text{Er}^{3+}:\text{Y}_2\text{SiO}_5$ are important to understand if we are to develop techniques to limit their effect. We can expect that, if they reach the edges of the crystal, the phonons will bounce due to the speed of sound in the crystal being much faster than in the surrounding helium. If the phonons have a long lifetime, then they will evenly distribute throughout the crystal and their density would be independent of where they were created. The hole fill-in at points spatially separated from the phonon creation site were measured and are shown in Section 4.2. The observed hole fill-in dropped over distance, indicating that the phonons are not bouncing sufficiently to become evenly distributed, and so have a mean free path smaller than the crystal.

The phonons created during this measurement were being emitted radially from the beam as it passed through the material. By taking the same measurement with a different beam shape, I can determine whether phonons are travelling in a straight line (ballistically). To induce a different spatial distribution of phonons, a cylindrical lens was used to change the shape of the beam. This lens only focuses the input light in one dimension, while the other dimension is unfocused, resulting in a plane of excitation. The cylindrical lens was

placed between the perturbation beam fibre and the beam splitter and rotated so that the plane was along the 3 mm length of the crystal and the beam could be translated along the 10 mm length of the crystal.

I took the same measurements using the plane of excitation as the line, which are shown in Figure 5.5. The two excitation shapes have very similar drop off with varied r , showing that the number of phonons hitting the atoms in the hole does not appear to vary with the different excitation shapes. This would not occur if the phonons are ballistic, as the two excitation shapes would have different trends. This means that phonons are not travelling in a straight line, and are being diffused as they are travelling through the crystal. This is different than findings in $\text{Er}^{3+}:\text{Y}_2\text{SiO}_5$ under low magnetic fields, where the phonons were found to be ballistic [37]. At low fields, the spin-lattice relaxation is weaker, so the phonons are less likely to diffuse through the erbium, so this would account for the observed difference in propagation. I will discuss potential mitigation techniques based on this information in the next chapter.

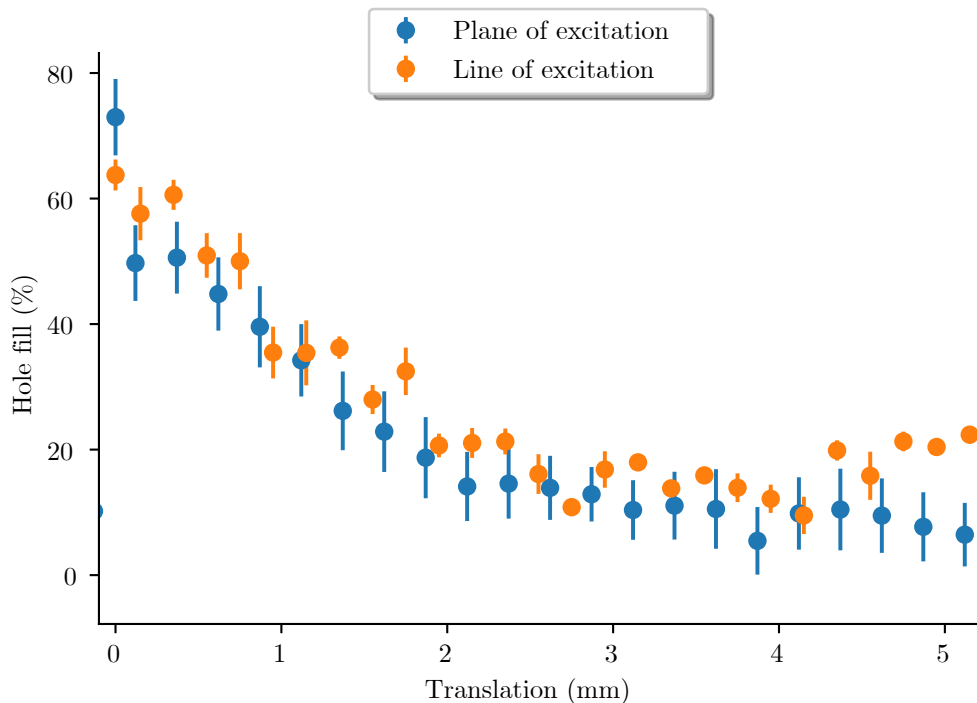


Figure 5.5: Hole fill-in versus beam translation. The orange points are from the beam travelling through the crystal, making a line of excitation, while the blue are from the beam being stretched into a line to form a plane of excitation.

5.4 Photon echoes

Although the hole burning measurements represent the ground state population redistribution, they are not sensitive to all possible interactions with non-equilibrium phonons. Holes are only sensitive to ions absorbing phonons, then remitting them at different frequencies to fall back into a different state. If the starting and finishing states are the same, there is no effect on the hole, but the coherence of the state is affected. This process

is a problem when information is stored on that state in a quantum memory protocol, because the act of absorbing and re-emitting a phonon adds random phase to the ion, and those random phase shifts degrade the stored quantum state. A measurement that would account for the total effect of the excitation induced phonons are photon echo measurements. As described in Chapter 2, photon echoes are used to determine coherence times as any population decay, and any changes in phase will reduce the echo amplitude.

To make a coherence time measurement, the photon echo sequence needs to be repeated with different delays between the $\pi/2$ and π pulses and the perturbation applied consistently for each measurement. The coherence time is then determined as the time constant off the echo decay curve with time. Other short-range excitation induced interactions are well known to affect phonon echoes, so I separated the beams by 0.5 mm to ensure that only the effect of phonons was being measured. I started by taking a base coherence time measurement with no perturbation, as shown in Figure 5.6. This measurement had a coherence time of 1.1ms, which matches the coherence times previously measured by James Stuart.

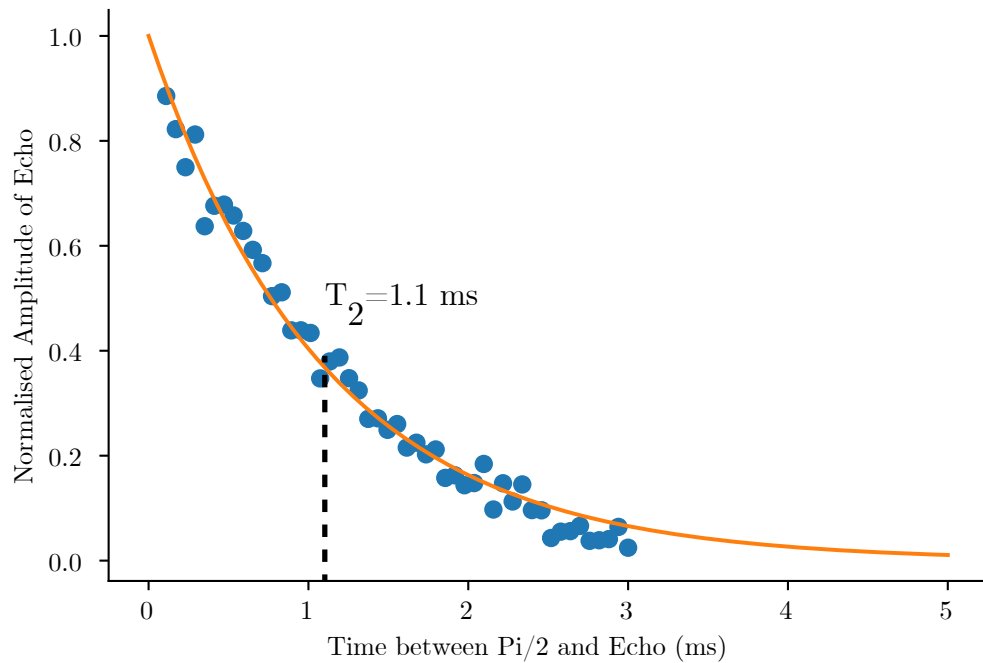


Figure 5.6: A coherence time measurement of the crystal without any perturbation. The measured coherence time was 1.1 ms which closely matches other coherence measures under the same conditions.

To see the effect of the non-equilibrium phonons, I applied the perturbation pulse throughout each photon echo measurement. This pulse was set to the maximum power of 8 mW to try to create a maximum number of phonons. The perturbed coherence measurement is shown in Figure 5.7. I measured the resulting coherence time to be 0.63 ms. As expected, this is a reduction in coherence time caused by the induced phonons creating random phase shifts and therefore decoherence. In a spatially multiplexed system of two memories with 0.5mm separation, this would reduce the storage times by 40%. If this material were

to be used in a multiplexed memory, either the input pulses need to be of lower intensity, the distance between modes needs to be increased, or a method needs to be developed to mitigate the phonons.

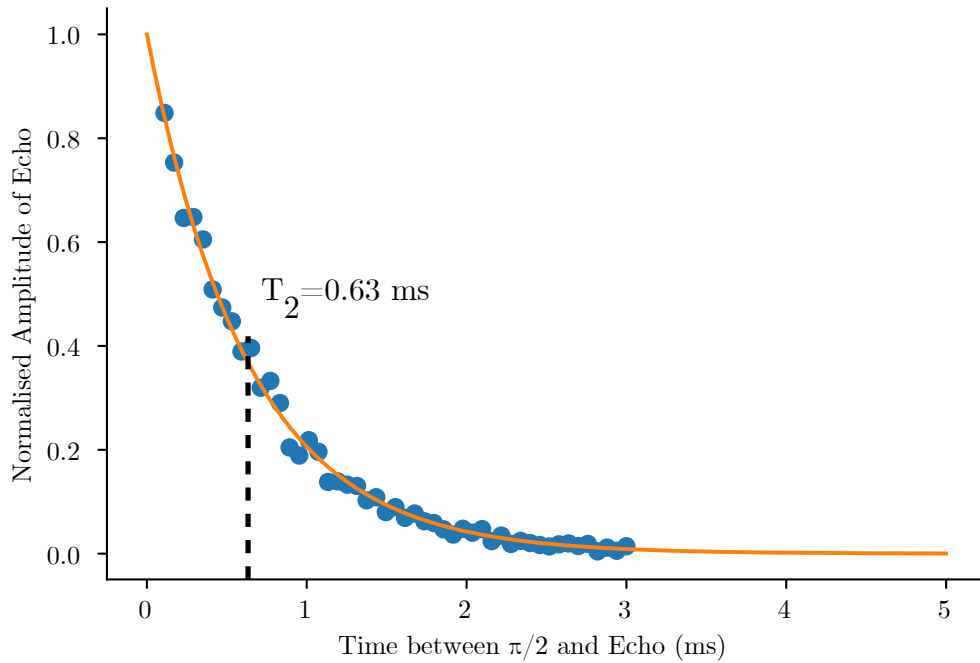


Figure 5.7: A coherence time measurement of the crystal while an 8 mW pulse is perturbing 0.5 mm away throughout the echo sequence. The measured coherence time was 0.63 ms, a reduction of 43%.

5.5 Phonon lifetime from echoes

Applying the perturbation pulse before performing the echo sequence gives information about the lifetimes of the phonon-excitation process. Photon echoes are only sensitive to events that occur during the echo sequence, as the atoms before the echo are not in a superposition state that can dephase. This requires exact times to start and stop the perturbation pulse, so I gated the perturbation laser with an acousto-optic modulator.

The experimental process was as follows. I set the delay between the two echo pulses to be fixed at 700 μ s and took a control measurement of the echo amplitude. 700 μ s was chosen as there was a clear photon echo for this time delay, with enough time to measure any changes caused by phonons. I then perturbed for 10 ms immediately before taking a photon echo measurement. This was repeated with increased delays between the perturbation turn off time and the echo measurement sequence.

The ratio of the perturbed and control echo with increasing perturbation delays is shown in Figure 5.8. At delays longer than 20 ms, the echo ratio is approximately 90%, with the ratio flattening without reaching unity. This is most likely due to light leaking through the perturbation beam AOM, even when the perturbation was ostensibly off. For these measurements, the perturbation pulse was gated using the AOM, which only blocks 99% of

the light. The remaining light would make a residual perturbation, lowering the amplitude of the echo. Nevertheless, the trend and timescale should be unaffected by this leakage. The echo ratio is minimised to the order of 20% when the delay between the perturbation and measurement is less than 1 ms, meaning we did not induce enough phonons to dephase the echo completely. The lifetime of the phonon process has two components - the timescale on which the phonons are created, and the lifetime of the phonons themselves. I can model the expected fill-in over time, assuming a linear relation between the phonon number and echo amplitude. This would give

$$r = r_{min} + r_{max} \left(1 - e^{-\frac{t}{T_1}} \right) \quad (5.1)$$

where r is the echo ratio, r_{min} is the minimum ratio, r_{max} is the maximum ratio, t is the time since perturbation and T_1 is the lifetime. Fitting r_{min} and r_{max} and using the measured lifetime of 9.2 ms [19], gave the model shown in Figure 5.8. This model assumes a phonon lifetime of zero, and the data only varies from this model slightly. This means that the phonon lifetime is significantly shorter than the 10 ms lifetime of the excited state, and that any diffusion of the phonons is over times significantly less than ms.

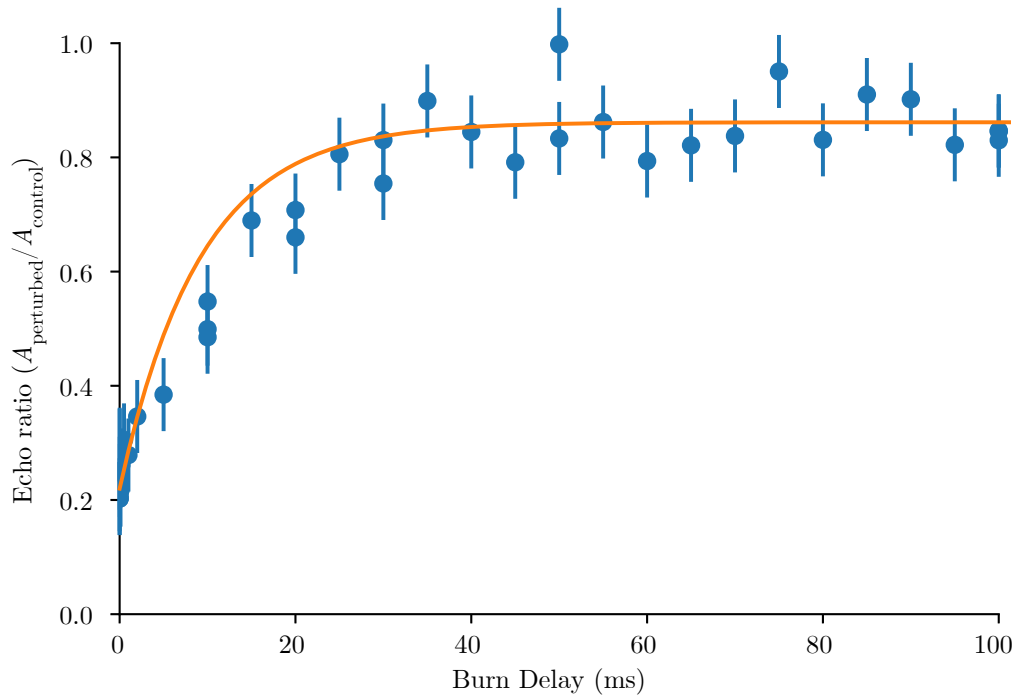


Figure 5.8: Photon echo ratio as a function of time since the end of the perturbation pulse. Each echo was compared to a control taken immediately before. The orange line is a fitted model assuming that there is a linear relation between the optical lifetime and reduction in echo amplitude.

5.6 Chapter Summary

In this chapter, I determined that the phonons induced by the perturbation are non-equilibrium phonons, as their decoherence depends on the perturbation frequency. I measured the linewidth of these phonons, finding that it was similar to the expected linewidth

given the inhomogeneous broadening. I used crystal field modelling to determine the frequency range of the different phonon transitions, finding that these matched the observations. I then took further measurements of the hole filling as the distance between the probe and perturbation changed but modified the beam shape to be a plane. Comparing these measurements with the previous measurements using a line of excitation, I concluded that the phonons are not travelling ballistically. Finally, I used photon echoes to show that the phonons reduce the coherence time of the atoms, that they are being created on the order of the excited state lifetime, and that the phonon lifetime is much shorter than the excited state lifetime.

Conclusions

In this thesis I have studied the generation of non-equilibrium phonons via optical excitation of erbium ions in Y_2SiO_5 . This was motivated by observations that increasing the optical excitation of ions during spin-polarisation resulted in a worsening of the spectral preparation. It was proposed that this was due to phonons, as they are an interaction induced by optical excitation, and I aimed to confirm if this was the case, and to characterise these phonons.

I started by ensuring that phonons were the interaction being observed. As phonons are the only interactions that propagate distances more than nanometres, I optically excited atoms millimetres away from a probed spectral hole. The variation of a spectral hole was measured as it provides a quantitative measure of the hyperfine redistribution, unlike the spin-polarised atoms. From these experiments, I observed that the hole was filled from millimetres away. To ensure that this was not due to the width of the perturbation beam overlapping the probed atoms, I modelled the effect of the beam edges, and found that the beam width effect was minimal. This confirmed that the perturbed atoms were spatially separated from those probed, and that phonons were being induced through optical excitation.

I then wanted to confirm the type of phonons. Phonons are either equilibrium and formed from the crystal heating and shifting the thermal distribution, or they are non-equilibrium, and emitted from excited atoms lowering in energy. This means that if equilibrium phonons are the observed interaction, they will be over a wide range of frequencies, while the non-equilibrium phonons will only be the frequency of the transition. To distinguish between these two types, I utilised the anisotropic Zeeman splitting of the two sub-sites to select the frequency separation between the probed and perturbed atoms by rotating the crystal. Taking measurements of the change in hole size at different frequency splittings, I observed that the hole stopped filling in when the two orientations were optically separated by 3 GHz. This meant the phonons being induced at this separation were non-resonant and therefore non-equilibrium.

Based on the optical frequency difference of the two sub-sites, I used crystal field modelling to determine that the measured phonons had an effect when their central frequency was offset from the probe atoms by up to 2.7 GHz. Since the phonons were likely from transitions between the lowest energy Zeeman levels, I used crystal field modelling to see if the total width of these transitions agreed with the 2.7 GHz observed. Between these levels there are 8 transitions with a frequency range of 2.9Hz. This corresponds with the observed phonon frequencies when inhomogeneous broadening is considered. Further work would

need to be undertaken to confirm the frequency of the phonons, including measurement of the hyperfine levels, as crystal field modelling only provides an approximation.

I then wanted to determine how the phonons are propagating through the crystal. Looking at the phonons' effect on spectral holes at different distances, I found that the effect decreased with large distances. As phonons will bounce if they reach the crystal edges, these findings indicated that the phonons have a short path length compared to the length of the crystal. I then considered if the phonons were travelling ballistically, by comparing how far the phonons could travel from two different emission shapes: a line of excitation, and a plane of excitation. If the phonons were ballistic, there would be a noticeable difference between these measurements. The two measurements had a similar drop off of phonon effect over distance. This indicated that the phonons were not ballistic, and therefore that the phonons are diffusing. A simulation of the diffusion process could be performed to determine whether the phonons are following a random walk, interacting with many erbium ions as they travel, or have some other path shape.

A limitation of the hole measurements used was that they do not show if the phonons cause any change in phase to the atom state. A way to measure this phase is by using a two-pulse photon echo and measuring the coherence time of the optical transition. I measured the coherence time with and without phonons being induced 0.5 mm away, observing a reduction of 43%. With confirmation that the phonons would affect a photon echo, I measured how long after the perturbation was stopped that they would still have an effect on the photon echo. I found that the phonons were created based on the lifetime of the excited state and did not observe any significant phonon lifetime effects. This indicated that the phonon lifetime, including diffusion processes, is orders of magnitude smaller than the 9.2 ms lifetime of the excited state.

6.1 Outlook and future directions

This thesis showed that non-equilibrium phonons are prevalent in $\text{Er}^{3+}:\text{Y}_2\text{SiO}_5$ and would need to be considered for any high information density quantum memory. Future directions stemming from this work are further characterisation of non-equilibrium phonons in $\text{Er}^{3+}:\text{Y}_2\text{SiO}_5$ (and other rare-earth crystals), and determining methods to counteract these phonons.

Much of the work in this thesis was performed by measuring the change of a spectral hole. Although this captures the redistribution of the hyperfine levels, it does not show any changes caused by the phase of the atoms - an important consideration for quantum memories. I started taking more information using photon echoes but had difficulties due to the size of the effect. Photon echoes are only affected by interactions made during the sequence (on the order of μs), unlike the hole measurements which will show a cumulative effect. This is illustrated by the relative sizes of the hole fill-in and photon echo effects that I saw: with pulses of 200 ms I was able to completely fill a spectral hole, whereas the maximum reduction in coherence time I saw was 40%. As such, there is a much smaller window for the phonons to be measured. Therefore, pulses that excite more atoms and therefore produce more phonons are needed. With such pulses, a useful study would be modifying the photon echo measurements with a third pulse. Three-pulse photon echoes give information about the population of the atoms and the phase simultaneously, which can be used to separate the dephasing and population redistribution processes. I began

preliminary measurements using three-pulse echoes, but could not excite enough atoms to see a measurable effect.

Measurements of the phonon lifetime were made difficult by the large difference in the optical lifetime and the phonon lifetime. To make more precise measurements of the phonon lifetime, coherent control of the optical state of the perturbation atoms could be used. Instead of exciting the atoms and waiting for them to spontaneously decay, a π pulse could be used to push the atoms into the excited state. The excited atoms would create phonons for a controllable amount of time (less than 9.2 ms), and then the process would be turned off by applying another π pulse. I attempted to measure the decoherence caused by a π pulse perturbation, however, was unable to excite enough atoms over the short π pulse time. This could be rectified by using a more powerful beam, or a wider frequency range.

Another limitation of the work in this thesis was the use of crystal field modelling to simulate the hyperfine levels and determine the range of phonon frequencies. The crystal field model is only an approximation, varying by hundreds of MHz from the hyperfine levels that have been measured in [39]. A research opportunity is to measure the energies of these other hyperfine levels. From these measurements, the phonon frequencies could be more accurately determined.

Modification of the experimental conditions could be used to determine more about the characteristics of the phonons. Experiments at lower magnetic fields would weaken the erbium spin-lattice interaction, and would also increase the phonon lifetime as they would be produced at lower frequencies. Another modification would be applying a magnetic field gradient to the crystal, which would vary the Zeeman splitting and therefore the resonant frequency of the phonons across the crystal. These measurements could be combined with a model of the diffusion to determine the shape of the phonons path and the number of erbium ions the phonons interact with.

Based on findings that phonons are diffusing through erbium ions, a number of methods could potentially mitigate the phonons. One option is to use larger, lower density crystals, lowering the probability that a phonon will propagate through an information storing ion. This could also be achieved by attaching a large crystal that the phonons can propagate through. Another solution is to apply a magnetic field gradient, shifting the frequency of each storage site to be non-resonant with the induced phonons of the next. My last solution is to use selective doping of the rare ion in the crystal. If the phonons have very short path lengths, sections of the crystal could be separated by walls without any dopant, where the phonon can diffuse into the phonon bath. Alternatively, these walls could be highly doped with erbium, increasing the probability of the phonon diffusing away from the memory. These are just some of the options that can be explored.

This project has many options for further investigation. The work so far will improve the efficient quantum memories being developed at the ANU, with further studies enhancing these developments.

Bibliography

- [1] H. J. Kimble. The quantum internet. *Nature*, 453(7198):1023–1030, June 2008.
- [2] H.-J. Briegel, W. Dür, J. I. Cirac, and P. Zoller. Quantum Repeaters: The Role of Imperfect Local Operations in Quantum Communication. *Physical Review Letters*, 81(26):5932–5935, December 1998.
- [3] Nicolas Sangouard, Christoph Simon, Bo Zhao, Yu-Ao Chen, Hugues de Riedmatten, Jian-Wei Pan, and Nicolas Gisin. Robust and efficient quantum repeaters with atomic ensembles and linear optics. *Physical Review A*, 77(6):062301, June 2008.
- [4] O. A. Collins, S. D. Jenkins, A. Kuzmich, and T. A. B. Kennedy. Multiplexed Memory-Insensitive Quantum Repeaters. *Physical Review Letters*, 98(6):060502, February 2007.
- [5] M. Razavi, M. Piani, and N. Lutkenhaus. Quantum repeaters with imperfect memories: Cost and scalability. *Physical Review A*, 80(3):032301, September 2009.
- [6] Miloš Rančić, Morgan P. Hedges, Rose L. Ahlefeldt, and Matthew J. Sellars. Coherence time of over a second in a telecom-compatible quantum memory storage material. *Nature Physics*, 14(1):50–54, January 2018.
- [7] Christoph Simon. Towards a global quantum network. *Nature Photonics*, 11(11):678–680, November 2017.
- [8] Morgan P. Hedges, Jevon J. Longdell, Yongmin Li, and Matthew J. Sellars. Efficient quantum memory for light. *Nature*, 465(7301):1052–1056, June 2010.
- [9] G. Hétet, J. J. Longdell, A. L. Alexander, P. K. Lam, and M. J. Sellars. Electro-Optic Quantum Memory for Light Using Two-Level Atoms. *Physical Review Letters*, 100(2):023601, January 2008.
- [10] Mikael Afzelius, Christoph Simon, Hugues de Riedmatten, and Nicolas Gisin. Multimode quantum memory based on atomic frequency combs. *Physical Review A*, 79(5):052329, May 2009.
- [11] Cyril Laplane, Pierre Jobez, Jean Etesse, Nuala Timoney, Nicolas Gisin, and Mikael Afzelius. Multiplexed on-demand storage of polarization qubits in a crystal. *New Journal of Physics*, 18(1):013006, December 2015.
- [12] Y-F Pu, N. Jiang, W. Chang, H-X Yang, C. Li, and L-M Duan. Experimental realization of a multiplexed quantum memory with 225 individually accessible memory cells. *Nature Communications*, 8(1):15359, August 2017.
- [13] Alexander I. Lvovsky, Barry C. Sanders, and Wolfgang Tittel. Optical quantum memory. *Nature Photonics*, 3(12):706–714, December 2009.

- [14] Manjin Zhong, Morgan P. Hedges, Rose L. Ahlefeldt, John G. Bartholomew, Sarah E. Beavan, Sven M. Wittig, Jevon J. Longdell, and Matthew J. Sellars. Optically addressable nuclear spins in a solid with a six-hour coherence time. *Nature*, 517(7533):177–180, January 2015.
- [15] Kate R. Ferguson, Sarah E. Beavan, Jevon J. Longdell, and Matthew J. Sellars. Generation of Light with Multimode Time-Delayed Entanglement Using Storage in a Solid-State Spin-Wave Quantum Memory. *Physical Review Letters*, 117(2):020501, July 2016.
- [16] John G Bartholomew. *Investigation of the Scalability of Rare-Earth-Ion Quantum Hardware*. PhD thesis, The Australian National University, 2014.
- [17] Thomas Böttger, C. W. Thiel, Y. Sun, and R. L. Cone. Optical decoherence and spectral diffusion at $1.5 \mu m$ in $\text{Er}^{3+}:\text{Y}_2\text{SiO}_5$ versus magnetic field, temperature, and Er^{3+} concentration. *Physical Review B*, 73(7):075101, February 2006.
- [18] O. Guillot-Noël, Ph. Goldner, Y. Le Du, E. Baldit, P. Monnier, and K. Bencheikh. Hyperfine interaction of Er^{3+} in Y_2SiO_5 : An electron paramagnetic resonance spectroscopy study. *Physical Review B*, 74(21):214409, December 2006.
- [19] Thomas Böttger. *Laser Frequency Stabilization to Spectral Hole Burning Frequency References in Erbium-Doped Crystals: Material and Device Optimization*. PhD thesis, Montana State University, 2002.
- [20] R. M. Macfarlane and R. M. Shelby. Coherent Transient and Holeburning Spectroscopy of Rare Earth Ions in Solids. In *Spectroscopy of Solids Containing Rare Earth Ions*. A. A. Kaplyanskii and R. M. Macfarlane, Eds., (North-Holland, 1987).
- [21] Sebastian P. Horvath, Jelena V. Rakonjac, Yu-Hui Chen, Jevon J. Longdell, Philippe Goldner, Jon-Paul R. Wells, and Michael F. Reid. Extending Phenomenological Crystal-Field Methods to C_1 Point-Group Symmetry: Characterization of the Optically-Excited Hyperfine Structure of $^{167}\text{Er}:\text{Y}_2\text{SiO}_5$. *Physical Review Letters*, 123(5):057401, July 2019.
- [22] S P Horvath. *High-Resolution Spectroscopy and Novel Crystal-Field Methods for Rare-Earth Based Quantum Information Processing*. PhD thesis, University of Canterbury, 2016.
- [23] F. Bloch. Nuclear Induction. *Physical Review*, 70(7-8):460–474, October 1946.
- [24] Rose Ahlefeldt. *Evaluation of a Stoichiometric Rare Earth Crystal for Quantum Computing*. PhD thesis, The Australian National University, 2013.
- [25] Nicolas Sangouard, Christoph Simon, Jiří Minář, Mikael Afzelius, Thierry Chanelière, Nicolas Gisin, Jean-Louis Le Gouët, Hugues de Riedmatten, and Wolfgang Tittel. Impossibility of faithfully storing single photons with the three-pulse photon echo. *Physical Review A*, 81(6):062333, June 2010.
- [26] Jérôme Ruggiero, Jean-Louis Le Gouët, Christoph Simon, and Thierry Chanelière. Why the two-pulse photon echo is not a good quantum memory protocol. *Physical Review A*, 79(5):053851, May 2009.

-
- [27] H. Y. Carr and E. M. Purcell. Effects of Diffusion on Free Precession in Nuclear Magnetic Resonance Experiments. *Physical Review*, 94(3):630–638, May 1954.
 - [28] L. Allen and J. H. Eberly. *Optical Resonance and Two-Level Atoms*. Interscience Monographs and Texts in Physics and Astronomy, v. 28. Wiley, New York, 1975.
 - [29] Mahmood Sabooni, Qian Li, Stefan Kröll, and Lars Rippe. Efficient Quantum Memory Using a Weakly Absorbing Sample. *Physical Review Letters*, 110(13):133604, March 2013.
 - [30] M Bonarota, J-L Le Gouët, and T Chanelière. Highly multimode storage in a crystal. *New Journal of Physics*, 13(1):013013, January 2011.
 - [31] Neil Sinclair, Erhan Saglamyurek, Hassan Mallahzadeh, Joshua A. Slater, Mathew George, Raimund Ricken, Morgan P. Hedges, Daniel Oblak, Christoph Simon, Wolfgang Sohler, and Wolfgang Tittel. Spectral Multiplexing for Scalable Quantum Photonics using an Atomic Frequency Comb Quantum Memory and Feed-Forward Control. *Physical Review Letters*, 113(5):053603, July 2014.
 - [32] Imam Usmani, Mikael Afzelius, Hugues de Riedmatten, and Nicolas Gisin. Mapping multiple photonic qubits into and out of one solid-state atomic ensemble. *Nature Communications*, 1(1):12, December 2010.
 - [33] A. Abragam and B. Bleaney. *Electron Paramagnetic Resonance of Transition Ions*. Oxford Classic Texts in the Physical Sciences. Oxford University Press, Oxford, 2012.
 - [34] R. M. Macfarlane and R. S. Meltzer. Optical dephasing of Pr^{3+} ions by nonequilibrium phonons in LaF_3 and YAlO_3 . *Le Journal de Physique Colloques*, 46(C7):C7–253–C7–257, October 1985.
 - [35] Y. S. Bai and R. Kachru. Nonequilibrium resonant-phonon-induced excess photon-echo dephasing. *Physical Review B*, 46(21):13735–13738, December 1992.
 - [36] Felix R. Graf, Alois Renn, Gert Zumofen, and Urs P. Wild. Photon-echo attenuation by dynamical processes in rare-earth-ion-doped crystals. *Physical Review B*, 58(9):5462–5478, September 1998.
 - [37] Rangga P. Budoyo, Kosuke Kakuyanagi, Hiraku Toida, Yuichiro Matsuzaki, William J. Munro, Hiroshi Yamaguchi, and Shiro Saito. Phonon-bottlenecked spin relaxation of $\text{Er}^{3+} : \text{Y}_2\text{SiO}_5$ at sub-kelvin temperatures. *Applied Physics Express*, 11(4):043002, April 2018.
 - [38] C. W. Thiel, W. R. Babbitt, and R. L. Cone. Optical decoherence studies of yttrium oxyorthosilicate Y_2SiO_5 codoped with Er^{3+} and Eu^{3+} for optical signal processing and quantum information applications at 1.5 microns. *Physical Review B*, 85(17):174302, May 2012.
 - [39] Miloš Rančić. *High Resolution Spectroscopy of Erbium Doped Solids*. PhD thesis, The Australian National University, 2018.
 - [40] Thomas Böttger, C. W. Thiel, R. L. Cone, and Y. Sun. Effects of magnetic field orientation on optical decoherence in $\text{Er}^{3+}:\text{Y}_2\text{SiO}_5$. *Physical Review B*, 79(11):115104, March 2009.